PRDM16 functions as a co-repressor in the BMP pathway to suppress neural stem cell proliferation

Li He[1], Jiayu Wen[2, *] and Qi Dai[1, *]

1 Department of Molecular Bioscience, the Wenner-Gren Institute, Stockholm University

2 Division of Genome Sciences and Cancer, The John Curtin School of Medical Research, The Australian National University

* Co-corresponding authors

Abstract

BMP signalling acts as an instructive cue in multiple developmental processes such as tissue patterning, stem cell proliferation and differentiation. It remains unclear how the same signalling input can be translated into a diverse range of cell-specific outputs. Here we have identified PRDM16 as a key regulator for BMP-induced neural stem cell (NSC) quiescence. We have determined genomic distribution of the SMAD4/pSMAD complexes in quiescent and proliferating NSCs and find that PRDM16 tethers the SMAD4 and pSMAD1/5/8 proteins at their co-bound genomic sites to prevent transcriptional activation of cell proliferation genes. Loss of *Prdm16* led to relocation of the SMAD complex to neighbouring genomic regions, leading to aberrant upregulation of BMP target genes. Such function of PRDM16 is also required for the specification of choroid plexus (ChP) epithelial cells. Using a single-cell resolution fluorescent *in situ* approach, we show that a SMAD/PRDM16 co-repressed gene, *Wnt7b*, and Wnt activity become upregulated in the *Prdm16* mutant ChP, which correlates with abnormally elevated cell proliferation. Together, our work defines the mechanism by which SMAD4 and pSMAD1/5/8 repress gene expression during the induction of cell quiescence and suggests a regulatory circuit composed of BMP and Wnt signaling and PRDM16 in the control of stem cell behaviors.

Introduction

Uncontrollable cell proliferation can lead to tumor growth, while premature differentiation can result in tissue degeneration. How stem cell proliferation and quiescence are regulated is a fundamental question in developmental and stem cell biology. BMP (Bone morphogenetic proteins) signaling is a key cell-signaling pathway that plays a role in inducing and maintaining stem cell quiescence. Additionally, BMP signaling is involved in numerous cell specification processes (Zhang and Li, 2005).

The ability of a single pathway to play a diverse range of roles relies on context-specific transcriptional outputs. SMAD4 is the common transcription factor that mediates BMP and TGF-β/Activin signaling. Upon BMP induction, SMAD4 associates with phosphorylated SMAD1/5/8, while in response to TGF-β/or Activin, it complexes with phosphorylated SMAD2/3. It is known that the SMAD protein complexes can both activate and repress target gene expression. However, the precise mechanism that determines the regulatory activity of SMADs and target gene selection remains unclear (Hill, 2016).

In the mammalian brain, BMP and Wnt signaling pattern the brain midline where an essential structure, the ChP, emerges. Neural epithelial cells at the site of presumptive ChP lose neural potential, and the majority of them exit cell cycle. Only a few cells at the boarder of the ChP primordium and cortical hem (CH) remain as slowly dividing ChP progenitors which expand the monolayered ChP epithelial cells (Liddelow et al., 2010). BMP signaling is essential for ChP epithelium specification. Conditional depletion of the BMP receptor *BMPr1a* diminishes ChP development (Hebert et al., 2002), while ectopic BMP was sufficient to transform neural progenitors into ChP cells (Watanabe et al., 2012). Wnt signaling peaking at CH is also required for ChPe cell specification (al, 2020). Conditional depletion of ß-Catenin resulted in defective ChP, while overexpression of ß-Catenin expands CH at the expense of the ChP epithelium. These observations suggest that the level of Wnt and BMP signaling needs to be tightly controlled to ensure proper cell specification.

The PR domain-containing (PRDM) family protein PRDM16 determines cell fate specification in various cell types (Aguilo et al., 2011; Baizabal et al., 2018; Chui et al., 2020; Chuikov et al., 2010; Inoue et al., 2017; Kajimura et al., 2008; Shimada et al., 2017). Consistent with its essential roles in normal development, mutation and dysregulation of *Prdm16* are linked with several human diseases including those identified in the patients with 1p36 chromosomal

79 aberrations. It has been shown that deletion of *PRDM16* has a causal role in cardiomyopathy
80 (Arndt et al., 2013), while co-amplification of *PRDM16* and *SKI* was shown to promote tumour
81 growth via suppressing TGF-β anti-proliferation activity in gastric cancer cells (Takahata et al.,
82 2009). Moreover, as a master regulator of the thermogenic gene expression program in brown
83 adipocytes, PRDM16 has been studied as a promising target to treat obesity and other metabolic
84 diseases (Horvath and Scheele, 2022).

85 PRDM16 has versatile functions at the molecular level. It regulates chromatin accessibility and
86 epigenetic states of its bound enhancers (Baizabal et al., 2018; He et al., 2021), and depending
87 on the associated cofactors, PRDM16 can repress or activate gene expression. This poses a
88 challenge when targeting PRDM16 is a therapeutic strategy in disease treatment because
89 undesired outcome may occur. Thus, it is important to get a full understanding of the regulatory
90 roles of this protein in each individual process.

91 In this study we have investigated the mechanisms that regulate the transition between stem
92 cell proliferation and differentiation. We show that *Prdm16* mutant ChP cells fail to transit from
93 proliferative to quiescent state, a similar phenotype to when BMP signaling is abolished (Hebert
94 et al., 2002). We dissected the molecular interaction of the SMAD4/pSMAD1/5/8 complex with
95 PRDM16 in the genome, and found that PRDM16 functions as a co-repressor for SMAD4 and
96 pSMAD1/5/8, by relocating the SMAD complex to distal repressive elements in the genes
97 encoding cell proliferation regulators. Finally, we validate that *Wnt7b* is a direct target co-
98 regulated by BMP signaling and PRDM16 in NSCs and that the elevated Wnt signaling
99 correlates with cell over-proliferation in the *Prdm16* mutant ChP. These findings uncover an
100 essential function of PRDM16 in stem cell regulation and BMP and Wnt signalling. PRDM16,

101

102

103

104

105

106

Results

Prdm16 is required for the specification of the ChP epithelium

BMP signaling starts to specify the presumptive ChP at embryonic day E10.5 in mice (Hebert et al., 2002) when *Prdm16* mRNAs become detectable in this region (**Fig. 1A**). Previously we reported that animals of the *Prdm16* knockout (KO) null allele, *Prdm16*^{cGT} (*cGT*), show severely reduced ChP structure (**Fig 1B)** (Bjork et al., 2010; He et al., 2021; Strassman et al., 2017). In the *Prdm16* KO mutant, expression of the ChP marker gene, *Ttr*, is not only reduced in the lateral ventricle (tChPs) but also in the fourth ventricle (hChP) (**Fig. 1C-D**), suggesting that the function of PRDM16 is not area-restricted but generally required for ChP development.

To assess the overall patterning of the CH and ChP region, we checked expression of *Wnt2b* and *BMP4* by conventional RNA *in situ* hybridization. The *Wnt2b* signal appeared normal in mutant brains compared with the controls at E11.5 and E12.5 (**Supplementary Fig. 1A**), suggesting that the area of CH is not affected by *Prdm16* deletion. Although the morphology of *Prdm16* mutant ChP epithelium looked defective, as it remained as thick as the neural epithelium, the level and range of *BMP4* expression in wild-type and mutant brains appeared comparable (**Supplementary Fig. 1A**). This result indicates that loss of *Prdm16* does not affect overall patterning of the medial-lateral region nor expression of *Wnt2b* and *BMP4*.

Neural epithelial cells in the ChP primordium rely on PRDM16 to exit cell cycle and loss neural potential

Next, we attempted to examine cellular changes underlying defective ChP in the *Prdm16* mutant. As the mutant ChP epithelium is thicker than the wild-type (**Fig. 1C-D**), we examined cell proliferation of the ChP cells by a 2-hour EdU labeling at E12.5. In control embryos from the same litter, the ChP cells were mostly EdU negative and transitioning into a monolayer, suggesting that these cells have exited cell cycle. By contrast, *Prdm16* mutant ChP cells remained highly proliferative (**Fig. 1E**).

To further check the property of *Prdm16* mutant ChP cells, we stained the control and mutant brain slices with the neuronal marker Doublecortin (Dcx). The control brain lacked Dcx positive cells in the ChP, suggesting that neural epithelial cells were specified into ChP epithelial cells and thus lost neural potential (**Fig. 1F**). However, there were a number of Dcx

positive cells lining along the basal side of the epithelium in the *Prdm16* mutant ChP, indicative of continued neurogenesis.

To further examine the property of ChP cells, we stained the brain sections with the stem cell marker SOX2. SOX2 is highly expressed in NSCs adjacent to the ChP epithelium, but its expression became significantly reduced in the presumptive ChP area (**Supplementary Fig. 1C**). However, such reduction was abolished in the *Prdm16* mutant.

Together, these results demonstrate that *Prdm16* depletion disrupted the transition from neural progenitors into ChP epithelia, leading to ectopic proliferation and neurogenesis. This phenotype is a reminiscence of the BMP pathway mutant, Foxg1-cre::loxp*Bmpr1a,* where ectopic cell proliferation was found in the developing ChP (Hebert et al., 2002). We then wondered whether PRDM16 interacts with the BMP pathway to restrict cell proliferation.

PRDM16 and BMP signaling collaborate to induce NSC quiescence

It is known that BMP signaling maintains adult NSC quiescence and that BMPs are sufficient to induce cultured proliferative NSCs into quiescence (Mira et al., 2010). To determine wether and how PRDM16 interacts with BMP signaling to regulate cell proliferation, we switched to using cultured primary NSCs (**Fig. 2A**). The PRDM16 protein is highly expressed in the nucleus of NSCs in embryonic brain tissues (**Fig. 1B**, and (He et al., 2021)). Unexpectedly, the protein became nearly undetectable when primary NSCs are cultured *in vitro* (**Supplementary Fig. 2A**) although *Prdm16* mRNA levels were still high (**Supplementary Fig. 2B**). This suggests that an unknown mechanism controls the stability and nuclear localization of PRDM16 *in vivo*. It was reported that post-translational modification of PRDM16 is an important regulatory switch for PRDM16 function in brown adipocytes (Wang et al., 2022). We speculate a similar mechanism used in NSCs in the brain. To overcome this issue and examine potential molecular function of PRDM16 in NSC proliferation and gene regulation, we infected primary NSCs with a lenti-viral construct that constitutively expresses *3xNSL_Flag_Prdm16* resulting. This cell line expresses high levels of Prdm16 mRNA and detectable PRDM16 protein in the nucleus and cytoplasm (**Supplementary Fig. 2A-B**). We referred this cell line as to *Prdm16_expressing (Prdm16_E)*. For comparison, we cultured NSCs from *Prdm16*_KO brains from the same developing stage and brain area.

165 Similar to previously reported (Mira et al., 2010), BMP4 was able to induce cell quiescence of
166 proliferative *Prdm16_E*xpressing NSCs, as indicated by the reduction in the number of mKi67-
167 stained or EdU-labeled cells (**Fig. 2B-C**). By contrast, many of the *Prdm16*_KO cells failed to
168 exit cell cycle after BMP4 addition, evidenced by less reduction of the mKI67 or EdU positive
169 cell population (**Fig. 2B-C**) and reduced *mKi67* mRNA levels measured by reverse-
170 transcription followed by quantitative PCR (RT-qPCR) assay (**Fig. 2D**).

171 BMP4 is able to induce ChP cell fate and ChP gene activation from neural progenitors *in vitro*
172 [5]. To examine whether PRDM16 facilitates the activity of BMP signaling in the induction of
173 ChP genes, we measured expression of *Ttr* using RT-qPCR. In NSCs that express *Prdm16*, we
174 detected an increase in *Ttr* mRNA expression, while the *Prdm16* KO NSCs and the NSCs
175 without the *Prdm16*_expressing construct show no induction at all (**Fig. 2E**).

176 Thus, as in ChP specification, both BMP signaling and PRDM16 are required for inducing NSC
177 quiescence and ChP gene expression. We then moved forward to examine the molecular
178 function of PRDM16 and BMP signaling in this context.

179 **BMP signaling and PRDM16 cooperatively repress cell proliferation genes to induce**
180 **quiescence.**

181 To determine how BMP signaling and PRDM16 regulate cell quiescence, we sought to
182 determine the transcriptional targets of SMAD4 and pSMAD1/5/8 in the condition of BMP4
183 versus no BMP4. We first tested a PRDM16 antibody and the available SMAD antibodies in
184 Cleavage Under Targets and Tagmentation (CUT&TAG) experiments, but none of the SMAD
185 antibodies worked. We then used chromatin immunoprecipitation followed by deep-sequencing
186 (ChIP-seq) to profile genomic binding sites for the SMAD proteins. As a control, we included
187 the antibody targeting SMAD3. Thus, our experiment settings allow profiling genomic binding
188 sites for PRDM16 and all three classes of SMAD proteins at the conditions with endogenous
189 BMPs and TGF-β/Activin and ectopic BMP4.

190 In *Prdm16_E* cells without BMP4, we identified a few hundred to thousand ChIP-seq peaks for
191 all three classes of SMAD proteins after normalizing to the input reads (FDR < 10%),
192 suggesting a modest level of endogenous BMP and TGF-β signaling in these cells (**Fig. 3A,**
193 **Supplementary Fig. 3**). Following BMP4 addition, pSMAD1/5/8 gained around 750-fold
194 more peaks, while the number of SMAD3 peaks increased less than three folds (**Fig. 3B**,

195 **Supplementary Fig. 3A**). Moreover, in cells treated with BMP4, the pSMAD1/5/8 peaks
196 largely overlap with the SMAD4 peaks, but not much with the SMAD3 ones (**Supplementary**
197 **Fig. 3B**). For instance, we found that there is pSMAD1/5/8 binding to two enhancers in the
198 intronic region of *Prdm16.* The binding intensity was dramatically increased in response to
199 BMP4 (**Supplementary Fig. 3D**). This indicates that *Prdm16* itself is a transcriptional target
200 of BMP signaling. Indeed, *Prdm16* mRNA levels can be elevated by BMP4 in wild-type but
201 not *Prdm16_KO* cells (**Supplementary Fig. 2B**). SMAD3 showed little ChIP-seq signal in the
202 enhancers of *Prdm16*. These results confirm that the response of pSMAD1/5/8 is specific to
203 BMP4, while SMAD3 is generally irresponsive to BMP4. The gained Smad3 sites may derive
204 from indirect effect of BMP signaling.

205 To assess the regulatory activity of SMAD4/pSMAD1/5/8 in NSCs, we determined the state of
206 transcription activation using H3K4me3 CUT&TAG signals at annotated gene TSS in BMP4-
207 treated and non-treated *Prdm16_E* cells. It is known that cell identity genes are marked by
208 extended breadth of H3K4me3 (Benayoun et al., 2014). We reasoned that compared to RNA-
209 seq that measures gene expression for all genes, changes in the H3K4me3 signal at the promoter
210 may bias toward cell identity genes between proliferation and quiescence states. We thus
211 determined all BMP4-repressed and activated genes, by measuring changes of the H3K4me3
212 CUT&TAG read coverage at annotated transcription starting sites (TSS) in BMP4-treated
213 *Prdm16_E* cells versus those non-treated, and identified 145 up-regulated and 184 down-
214 regulated SMAD target genes (**Fig. 3B**) ($P<0.01$).

215 To identify the function of genes regulated by BMP signaling, we performed gene ontology
216 (GO) analyses for the genes that changed expression in response to BMP4 in *Prdm16_E* cells
217 (see Methods). Remarkably, only the downregulated genes (BMP4-repressed genes) show
218 significantly enriched functional categories, and nearly all GO terms are related to cell
219 proliferation/cell cycle (**Fig. 3C**). A recent study reported that BMP2-induced genes are mostly
220 enriched for neuronal and astrocyte differentiation (Katada et al., 2021), while our analysis did
221 not identify these categories. The discrepancy may derive from different BMP ligands (BMP4
222 versus BMP2), difference in NSC culture, as ours was from E13 instead of E11 and E14, or
223 different profiling methods, H3K4me3 versus RNA-seq.

224 To identify PRDM16-repressed and activated genes in the condition of active BMP signaling,
225 we called changes of H3K4me3 coverage at TSSs in BMP4-treated *Prdm16_KO* cells versus
226 BMP4-treated *Prdm16_E* cells. There were about twice as many up-regulated genes as down-

227 regulated genes (**Fig. 3D**), suggesting that the cooperative activity of PRDM16 and BMP
228 signaling mainly represses target gene expression. To identify the common targets repressed by
229 PRDM16 and BMP signaling, we overlapped the 184 genes repressed by BMP4 and the 240
230 genes repressed by PRDM16, and identified 31 common ones. These 31 genes all display low
231 H3K4me3 coverage in *Prdm16_E* cells with BMP4 but higher H3K4me3 signal in both
232 *Prdm16_KO* cells treated with BMP4 and *Prdm16_E* cells without BMP4 (**Fig. 3E).**

233 We further confirmed that the change of H3K4me3 intensity at the *Wnt7b* promoter faithfully
234 recapitulated the change of *Wnt7b* mRNA levels by using RT-qPCR (**Fig. 3F-G**). As a negative
235 control, the TGF-β pathway target gene *Cdkn1a* encoding the cell cycle inhibitor *p21* showed
236 unchanged H3K4me3 coverage between BMP4 treated and non-treated cells and between
237 *Prdm16_E* and *KO* cells, suggesting that neither PRDM16 nor BMP signaling affects
238 expression of *Cdkn1a* in NSCs.

239 **PRDM16 assists genomic binding of the BMP pathway transcription factors**

240 To determine how PRDM16 interacts with BMP signaling, we integrated the PRDM16
241 CUT&TAG with the SMAD ChIP-seq data and focused on assessing how PRDM16 influences
242 genomic binding of the SMAD proteins.

243 The SEACR peak caller software (Meers et al., 2019) identified 3337 and 7639 PRDM16
244 CUT&TAG common peaks from four replicates of the BMP4-treated and non-treated
245 *Prdm16_E* samples (FDR < 10%, see Methods) respectively, representing PRDM16-bound
246 genomic sites at these two conditions (**Fig. 4A**). The samples from *Prdm16_KO* cells
247 completely lack these sites, validating the specificity of the PRDM16 CUT&TAG signal (**Fig.**
248 **4B**). There are 5936 lost and 1634 gained PRDM16 CUT&TAG peaks upon BMP4 treatment,
249 suggesting that PRDM16 regulates a distinct subset of genes in proliferating versus quiescent
250 NSCs.

251 In the overlapping analyses (see Methods), we found that more than 50% of SMAD4 and
252 pSMAD1/5/8 binding peaks are consistent in *Prdm16_E* and *Prdm16_KO* cells
253 (**Supplementary Fig. 4A-B**), suggesting that deletion of *Prdm16* does not affect general
254 genomic binding ability of the SMAD4/pSMAD1/5/8 proteins. In *Prdm16_E* cells with BMP4,
255 most of PRDM16 CUT&TAG peaks overlap with the SMAD4 and pSMAD1/5/8 peaks, but
256 not much with SMAD3 (**Supplementary Fig. 4A-C**), suggesting that PRDM16 mainly

257 collaborates with the SMAD4/pSMAD1/5/8 complex but not the SMAD3/SMAD4 complex in
258 cells with BMP4.

259 Interestingly, the enrichment of SMAD4 and pSMAD1/5/8 at the PRDM16 co-bound sites
260 became significantly lower in *Prdm16_KO* cells than that in *Prdm16_E* cells (**Fig. 4C**)
261 (P=2.5E-6, and P=4.7E-3, respectively, two-tailed *t*-test). This result indicates that SMAD
262 binding to the PRDM16/SMAD co-bound sites depends on PRDM16. As a control, the sites
263 without PRDM16 co-binding did not show such change (P>0.05).

264 To validate the co-binding of SMAD4 and PRDM16, we selected the candidate loci of *Wnt7b*
265 and *Id1* (**Fig. 4D-E**). We first confirmed that SMAD4 and PRDM16 simultaneously bind to the
266 same DNA molecules by using sequential ChIP-qPCR with the PRDM16 antibody in the first
267 round of IP and the SMAD4 antibody in the second IP at the *Wnt7b* and *Id1* gene loci
268 (**Supplementary Fig. 4D**). SMAD4 displayed higher enrichment in the chromatin pulled by
269 the PRDM16 antibody compared to that by the IgG control. We also validated reduced SMAD
270 binding at the SMAD/PRDM16 co-bound site by ChIP-qPCR with the SMAD4 antibody in
271 *Prdm16_E* and *Prdm16_KO* cells. SMAD4 binding became consistently weaker in the mutant
272 in two biological replicates (**Fig. 4F-G**). Thus, PRDM16 enhances genomic binding of the
273 SMAD proteins to specific genome regions.

274 We then wondered what distinguishes the regions co-bound by SMADs and PRDM16 from
275 those only bound by SMADs. To this end, we checked whether there is any intrinsic difference
276 between SMAD-bound regions with and those without PRDM16 binding. It has been shown
277 that SMAD4 can bind two major types of DNA motifs (Hill, 2016): together with pSMAD1/5/8
278 or pSMAD3, SMAD4 may bind to a palindromic motif, GTCTAGAC or direct repeats of
279 GTCT like GTCTGTCTGTCT (Dennler et al., 1998; Wong et al., 1999; Zawel et al., 1998);
280 together with pSMAD1/5/8, SMAD4 associates with GC-rich SBEs (SMAD-binding elements)
281 including GGCGCC-AN4-GNCV and GRCGNCNNNNNGTCT (Gao et al., 2005;
282 Pyrowolakis et al., 2004; Weiss et al., 2010). To determine how PRDM16 may influence
283 binding site selection of SMADs, we calculated occurrence frequency of each of these motifs
284 in binned SMAD4 ChIP-seq peaks from *Prdm16_E* cells treated with BMP4 (bin 1 to 5 with
285 low to high peak scores, **Fig. 4H**). Interestingly, the palindromic motif is the most enriched,
286 and its occurrence frequency increases with peak scores but becomes lower in the SMAD4
287 peaks without PRDM16 co-binding. The frequency of the motif with three copies of GTCT also
288 increases with higher SMAD4 peak scores, but there is no reduction in regions without

289 PRDM16 binding. The two GC-rich motifs show a different trend: they are not as highly
290 enriched, their frequencies do not increase with higher SMAD4 peak scores, and the occurrence
291 frequency in PRDM16 co-bound regions is either comparable to or even lower than the regions
292 without PRDM16 binding. This result suggests that PRDM16 separate the
293 SMAD4/pSMAD1/5/8 proteins into two types of genomic regions, one enriched for the
294 palindromic motif and the other with the GC-rich motifs, by tethering the SMAD complex to
295 the regions enriched of the palindromic motif.

296 **SMAD4 and pSMAD1/5/8 switch genomic locations in the absence of PRDM16**

297 Our careful inspection on the *Wnt7b* and *Id1* loci surprisingly revealed that there are multiple
298 ectopic SMAD4 and pSMAD1/5/8 peaks in the *Prdm16* mutant sample (arrow-indicated peaks
299 in **Fig. 5A-B**). We then globally assessed the extent of ectopic SMAD binding surrounding the
300 SMAD/PRDM16 co-bound sites by quantifying differential SMAD binding intensity between
301 *Prdm16_KO* and *Prdm16_expressing* cells (**Fig. 5C,** FDR < 10%). In agreement with the
302 metaplots (**Fig. 4C**), all of the SMAD/PRDM16 co-bound sites (blue dots) showed reduced
303 ChIP-seq read coverage in *Prdm16_KO* cells. By contrast, the flanking regions within the
304 200kb range of a co-bound site (red dots) displayed a trend of increase of SMAD binding in
305 *Prdm16_KO* cells. This result agrees with the aforementioned motif analysis that PRDM16
306 helps to localize the SMAD complex at specific genomic regions, and it also suggests that
307 without *Prdm16*, the SMAD factors are partly redirected to neighboring genomic regions.

308 **AP1 is the potential co-factor that interacts with relocated SMAD proteins**

309 We intended to find out how SMAD4 and pSMAD1/5/8 relocate to ectopic sites in the absence
310 of *Prdm16*. By running *de novo* motif discovery (see Methods), we identified a number of
311 significantly enriched DNA motifs from pSMAD1/5/8 and SMAD4 ChIP-seq peaks in
312 *Prdm16_E* and *Prdm16_KO* cells (**Fig. 5D-E**). Interestingly, in addition to the known SMAD
313 motifs, the only other motif identified in both pSMAD1/5/8 and SMAD4 peaks from
314 *Prdm16_KO* cells but not *Prdm16_expressing* cells is the AP1 motif. Furthermore, the AP1
315 motif is more frequently found in the pSMAD1/5/8 and SMAD4 regions lacking PRDM16
316 binding than those with PRDM16 binding (Supplementary **Fig. 4E**). The interaction between
317 the AP-1 complex with the SMAD proteins was reported previously (Zhang et al., 1998). Our
318 result implies that AP-1 is a potential cofactor for the SMAD proteins in the absence of *Prdm16*.
319 To validate this finding, we performed ChIP-qPCR with an antibody against c-FOS, one of the

320 subunits of AP1, on *Prdm16_E* and *KO* cells. Supporting the global analyses, c-FOS is enriched
321 in the Smad4-bound regions at the *Wnt7b* and *Id3* loci in the *Prdm16_KO* condition (**Fig. 5F-**
322 **G**). There is little c-FOS binding to these regions in cells expressing *Prdm16*, suggesting that
323 there is cooperativity of SMAD and AP-1 which facilitates each other's binding when PRDM16
324 is absent. Alternatively, PRDM16 may suppress genomic accessibility of these regions for
325 SMAD and AP-1 proteins, a function we reported for PRDM16 in cortical NSCs (He et al.,
326 2021).

327 Together, our genomic data and validation suggest an enhancer switch model (**Fig. 5H)**:
328 PRDM16 assists SMAD protein binding to repressive cis-regulatory elements that are enriched
329 for GTCTAGAC palindromic motifs; loss of PRDM16 results in genomic relocation of SMAD
330 proteins, presumably via the association with coactivators such as AP1; the consequence of
331 SMAD relocation is de-repression of cell proliferation regulators.

332 **SMADs and PRDM16 co-regulated genes in NSCs are repressed in the developing ChP**

333 Next, we intended to examine whether the genes co-regulated by PRDM16 and BMP signaling
334 in the NSC culture are involved in ChP development, an *in vivo* setting where BMP signaling
335 (Hebert et al., 2002) and PRDM16 (**Fig. 1**) restrict NSC proliferation. To address this, we first
336 examined expression of these genes in the developing mouse brain by taking advantage of the
337 published single cell RNA-seq (scRNA-seq) data (La Manno et al., 2021). We selected a
338 number of cell clusters based on marker gene expression from E12.5 mouse brain, including
339 the ChP epithelial cell clusters (*Ttr* positive), CH clusters (BMP4 positive but *Ttr* negative) and
340 a few forebrain-specific radial glia (RG) clusters (Sox2/Hes5 positive) (**Fig. 6A**). Among the
341 31 genes, six show no expression, and five have weak expression in the examined clusters
342 (**Supplementary Fig. 5A**). The remaining twenty genes display a moderate to high level of
343 expression in at least one cluster. Interestingly, they are generally more lowly expressed in the
344 ChP clusters than the neural clusters (CH and RG ones) (**Fig. 6A**), suggesting that expression
345 of these genes is suppressed in the ChP. To identify which of these genes are directly regulated
346 by PRDM16, we performed CUT&TAG assays using the PRDM16 antibody on dissected
347 dorsal midline tissue that mainly contains CH and the ChP (**Fig 6B** and **Supplementary Fig.**
348 **5B**) and identified 3238 common peaks from three biological replicates. We then manually
349 inspected the 31 gene loci for PRDM16 CUT&TAG peaks pairing with the target gene TSS
350 using the browser Embryonic Mouse Brain Epigenome Atlas (Rhodes et al., 2022). This

351 conformed that most of these genes have at least one PRDM16 binding peak in their promoter-
352 linked enhancers (Text in black, **Fig. 6A** and **Supplementary Fig. 5A**).

353 Among these genes, *Wnt7b* is of particular interest, because the level of Wnt signaling was
354 shown to be critical for ChP specification (Parichha et al., 2022), and Wnt signaling promotes
355 proliferation of NSCs (Kalani et al., 2008). Although the sequencing coverage looks sparser
356 compared to that from NSC culture, there are two PRDM16 binding peaks identified within the
357 *Wnt7b* region (**Fig 6C**). The intronic peak is unique to the dorsal midline tissue, suggesting that
358 this enhancer may be specifically regulated in the developing ChP. Thus, *Wnt7b* is a potential
359 target of PRDM16 in the developing ChP.

360 **PRDM16 represses *Wnt7b* and Wnt activity in the developing ChP**

361 We sought to determine whether PRDM16 regulates Wnt gene expression in the developing
362 ChP. In addition to *Wnt7b*, there are several other Wnt ligands expressed in the CH and ChP
363 region (Harrison-Uy and Pleasure, 2012). For example, *Wnt3a* is expressed in the dorsal-
364 midline region but not in the forebrain, which explains why it was not identified from the
365 forebrain-derived NSC datasets. Although there is no PRDM16 binding peak within the *Wnt3a*
366 locus in the CUT&TAG data from NSCs, there is a peak in the intronic region of *Wnt3a* in the
367 data from the dorsal midline tissue (**Supplementary Fig.5C**). This suggests that it is also a
368 direct target of PRDM16. We thus examined the scRNA-seq data (La Manno et al., 2021) and
369 confirmed that multiple components in the Wnt and BMP pathways are present in the CH and
370 ChP clusters (**Supplementary Fig.5D**). To systematically measure expression changes of Wnt
371 and BMP signaling components in the *Prdm16* mutant brain, we applied a multiplexed
372 fluorescent *in situ* approach, Single-Cell Resolution in Situ Hybridization On Tissues
373 (SCRINSHOT) (Sountoulidis et al., 2020). In this method each mRNA molecule is hybridized
374 with three gene-specific padlock probes and visualized by florescent dye-conjugated detection
375 probes. A dot of fluorescent signal corresponds to one mRNA molecule, allowing quantitative
376 measurement of gene expression in single cell resolution.

377 We designed probes for ten Wnt and five BMP pathway components as well as cell-type
378 specific markers (the ChP marker gene *Ttr* and *Foxj1*, the neural progenitor markers *Sox2*, *Hes5*
379 and *Zbtb20,* and the neuronal marker Ngn2) (**Fig. 7**) and conducted SCRINSHOT in three pairs
380 of control and Prdm16 mutant brains.

381 In the control brain, *Ttr* and Foxj1 are highly expressed in the ChP epithelium at E11.5 and
382 E12.5, and several Wnt (*Wnt2b*, *Wnt7b*, *Wnt5a*, *Wnt3a*, *Fzd10* and *Axin2*) and BMP
383 components (*BMP4* and *BMP7*) display certain tissue specificity: the Wnt genes are more
384 enriched at CH while the BMP genes are more at the ChP. The representative images from
385 E11.5 samples are presented in **Fig. 7 A-B**. Except *Wnt2b*, the other tested *Wnt* genes also
386 display low expression in the ChP cells, consistent with the notion that Wnt signaling is present
387 and required at the ChP (Parichha et al., 2022).

388 Next, we quantified expression changes of these genes in *Prdm16* mutant CH and ChP cells.
389 As expression of *Wnt2b* was relatively unchanged in the mutant (**Supplementary Fig. 1** and
390 **Fig. 7A**), we used *Wnt2b*-expressing cells to define the CH cells and those expressing *Ttr* to
391 define ChP cells in the wild-type brain slice. There were about 110 cells in each region of one
392 brain slice. Because the mutant brain slice showed little *Ttr* signal, we only used the *Wnt2b*-
393 expressing cells to define the anterior border between CH and neocortex and included 110 cells
394 under the border for the CH cells, and the further 110 cells for the mutant ChP cells, as shown
395 in the images with DAPI and cell outlines (**Fig. 7A and 7D**). We then measured the dot count
396 of each gene in these 220 cells in each sample and summarized the changes calculated from
397 three pairs of animals in the violin plots (**Fig. 7 C** and **Supplementary Fig. 6A**). Expression of
398 *Ttr* and *Foxj1* is severely reduced, while *Sox2*, *Hes5* and *Ngn2* all become upregulated in the
399 mutant ChP, indicating a fate transformation of ChP epithelial to neural cells. This fully agrees
400 with our immunostaining and conventional *in situ* results (**Fig. 1** and **Supplementary Fig. 1**).
401 Similar to BMP4, other BMP components we tested including *BMP7*, *Smad6*, *Smad7 and Nog*
402 are unchanged, suggesting that PRDM16 is not an upstream regulator of the BMP pathway.

403 Remarkably, *Wnt3a* and *Wnt7b* are significantly upregulated in the *Prdm16* mutant ChP (**Fig.**
404 **7B-E** and **Supplementary Fig. 6A-C**). The Wnt target gene *Axin2* is also upregulated,
405 indicating that the activity of Wnt signaling is aberrantly elevated in the *Prdm16* mutant ChP.
406 Thus, the normal function of *Prdm16* represses WNT signaling in the developing ChP.

407 **Levels of Wnt activity correlate with cell proliferation in the developing ChP and CH**

408 As *Prdm16* mutant ChP cells showed elevated Wnt signaling (**Fig. 7 A-C**) and ectopic cell
409 proliferation (**Fig. 2**), we assessed the relationship between Wnt signaling and cell proliferation
410 in the ChP and CH at E12.5. We defined cell proliferation state using expression levels of
411 *mKi67* by quantifying the number of dots of *mKi67* SCRINSHOT signal in 110 CH and 110

412 ChP cells in each wild-type and mutant sample. There is a significant increase of *mKi67*
413 expression in *Prdm16* mutant ChP cells at E12.5 (**Fig. 7F**), accompanied by significantly
414 increased *Wnt3a*, *Wnt7b* and *Axin2* levels (**Fig. 7F** and **Supplementary Fig 6B-C**). In contrast,
415 there is little or no increase of *mKi67* signal in the mutant CH, suggesting that the effect of
416 PRDM16 is mainly cell-autonomous. We then performed linear regression and Pearson
417 correlation analyses to see correlations between ChP markers, BMP and Wnt genes.
418 Interestingly, the level of *Axin2* best correlates the level of m*Ki67*, even better than that with
419 other Wnt genes in both wild-type ($r = 0.46$; $p < 2.2$ E-35) and mutant ($r= 0.56$; $p < 1.6$ E-55)
420 CH and ChP cells **(Fig. 7G** and **Supplementary Fig. 6D**). This result suggests that Wnt activity
421 is responsible for cell proliferation in the CH and ChP region. In line with this finding, it was
422 shown that ectopic Wnt signaling converts ChP cells into proliferative CH neural cells
423 (Parichha et al., 2022).

424 Similarly, in the 4th ventricle, *Prdm16* deletion caused severe ChP defects (**Fig. 1D** and
425 **Supplementary Fig. 7**). In this region from wild-type brains, *Wnt7b* showed little expression,
426 while *Wnt3a* and *Wnt1* appeared abundant in the two areas flanking the hChP. Interestingly,
427 these two genes and *mKi67* all became ectopically expressed in *Prdm16* mutant ChP cells. Thus,
428 PRDM16 also suppresses Wnt signaling in the hindbrain ChP. Taken together, our results
429 suggest that specification of the ChP epithelium requires a process transitioning proliferating
430 NSCs into quiescence, and that this process is mediated by a suppressive role of PRDM16 on
431 Wnt signaling.

432

433

434

435

436

437

438

439

Discussion

In this study we reveal a new molecular mechanism by which BMP signaling induces cell quiescence and represses gene expression. We find that PRDM16 acts as a tethering factor to localize the SMAD4/pSMAD1/5/8 complex at specific genomic sites and facilitate the repressive role of the SMAD proteins. The genes co-repressed by PRDM16 and BMP signaling include those encoding Wnt pathway ligands and other cell proliferation regulators.

Combinatory activities of morphogens are exploited throughout animal development and tissue homeostasis. The crosstalk between BMP and WNT signaling is complex as it can be synergistic or antagonistic (Itasaki and Hoppler, 2010). Surprisingly, both types of effects exist in the specification of ChP epithelium. Here BMP signaling induces NSC quiescence, as evidenced by the presence of ectopic proliferating cells at the ChP in *Bmpr1a* mutant mice (Hebert et al., 2002), while Wnt signaling promotes proliferation since the gain-of-function condition of beta-Catenin phenocopies *Bmpr1a* mutant animals (Parichha et al., 2022). On the other hand, adding a low dose of Wnt activator to cell culture medium enhances programing efficiency of ChP epithelial cells induced by BMP4 (Pellegrini et al., 2020), and loss-of-function of beta-Catenin resulted in under-developed ChP structure (Parichha et al., 2022), suggesting that BMP and WNT signaling collaborate to promote ChP epithelial cell differentiation. Our work demonstrated that PRDM16 ensures the right balance of BMP and Wnt activity by maintaining a low level of Wnt gene expression in the developing ChP.

PRDM16 was shown to physically interact with SMAD3 in *in vitro* assays (Warner et al., 2007) and antagonize TGF-β induced cell cycle arrest (Takahata et al., 2009). However, we failed to detect a stable PRDM16/SMAD4/pSMAD1/5/8 complex in co-immunoprecipitation experiments (data not shown). Instead, we found that PRDM16 and SMAD4 bind to the same DNA molecule in the sequential ChIP assay, suggesting that the cooperative activity of SMAD4 and PRDM16 occurs at their co-bound *cis* regulatory loci. We further identified the intrinsic difference of the DNA sequences bound by SMADs when associated with PRDM16 compared to those without PRDM16, with SMADs preferentially binding to the palindromic motif in the presence of PRDM16 and to the classic GC-rich SBE motifs in the absence of PRDM16. This provides a mechanistic insight into how SMADs switch its regulatory activity from repressing to activating gene expression. In contrast to the previous report indicating that PRDM16 antagonized the anti-proliferation activity of TGF-β and SMAD3, we show here that PRDM16 collaborates SMAD4 and pSMAD1/5/8 to suppress proliferation genes, which is consistent

472 with the quiescence-inducing function of BMP signaling. Moreover, while it was reported that
473 PRDM16 promotes Wnt signaling by stabilizing nuclear beta-Catenin in the craniofacial tissue
474 (Shull et al., 2022), we detected the opposite outcome in the ChP and cultured NSCs, with
475 ectopic WNT gene expression in the absence of *Prdm16*, suggesting that PRDM16 represses
476 Wnt genes in these contexts. Notably, PRDM16, Wnt and BMP co-exist in various
477 developmental settings, such as craniofacial development (Bjork et al., 2010; Nie et al., 2006;
478 Shull et al., 2022), heart formation (Arndt et al., 2013; Gessert and Kuhl, 2010; van Wijk et al.,
479 2007), limb patterning (Bjork et al., 2010; Geetha-Loganathan et al., 2008; Robert, 2007), adult
480 intestinal stem cells (He et al., 2004; Korinek et al., 1998; Stine et al., 2019) *etc*. We speculate
481 a similar regulatory circuit is used in some, if not all, of these settings.

482 ChPe epithelial cells derive from proliferating NSCs, without intermediate fate-commitment
483 steps. This property endows ChP cells with higher plasticity and makes them more vulnerable
484 to abnormal genetic and cellular change, to which high occurrence frequency of ChP tumors in
485 fetuses and young children may be attributed (Wolff et al., 2002). As an essential brain structure,
486 the ChP releases cerebrospinal fluid (CSF) and acts as a brain-blood barrier (Johansson, 2014;
487 Lehtinen et al., 2013; Lun et al., 2015). Its dysfunction has been linked with several types of
488 human diseases including hydrocephalus, Alzheimer's disease, multiple sclerosis (Lun et al.,
489 2015). Deepening our knowledge on the development of ChP will provide new insights into
490 potential therapeutics to prevent or treat ChP tumors and other ChP-related diseases.

491 **Footnote**: a study on the antagonism between PRDM16 and SMAD4 was published on Feb 24,
492 2023 (Hurwitz, 2023) after we posted our manuscript at BioRxiv and during our submission
493 process.

494

495

496

497

498

499

500 **Materials and methods**

501 **Animals**

502 All animal procedures were approved by Swedish agriculture board (Jordbruks Verket) with
503 document number Dnr 11553-2017 and 11766-2022. The *Prdm16*^{cGT} mice (Strassman et al.,
504 2017) were maintained by outcrossing with the FVB/NJ line.

505 **In situ hybridization**:

506 To make probes for conventional RNA in situ hybridization, genomic regions covering one
507 exon or full-length cDNA were PCR amplified to generate fragments with restriction enzyme
508 overhangs. The sequences of all oligos were included in Supplementary table 1. The fragments
509 were inserted to the pBluescript SK(II) vector. In vitro transcription was performed as
510 previously described (He et al., 2021). The mouse brains at defined ages were dissected and
511 fixed for 12 hours in 4% PFA, dehydrated in 25% sucrose, cryoprotected and embedded in
512 O.C.T. The brain samples were then sectioned at 18 μm thickness on Leica cryostats CM3050s.
513 RNA *in situ* hybridization was performed using digoxigenin-labeled riboprobes as described
514 previously. Detailed protocols are available upon request. Images were taken using a Leica
515 DMLB microscope.

516 **Immunostaining**

517 Immunostaining was done according to standard protocols as previously used (Dai et al., 2013a).
518 For EdU labeling, EdU (5-ethynyl-2′-deoxyuridine) (5-20 μg/g of body weight) was injected
519 into the peritoneal cavity of pregnant mice. EdU incorporation was detected with the Click-iT
520 assay (Invitrogen) according to the manufacturer's instructions. Imaging was done on Zeiss
521 confocal microscope. ZEN (ZeissLSM800), ImageJ (NIH) and Photoshop (Adobe) were used
522 for analysis and quantification.

523 **NSC culture**

524 Control and mutant embryonic cortices from E13.5 animals were dissected and dissociated into
525 single cell suspension and digested with Acutase (Sigma). Cells were maintained in
526 proliferation media (STEMCELL Technologies). Lentivirus expressing Flag-Prdm16 and a
527 puromycin resistant gene in the pCDH vector was produced in 293-ft cells and used to infect a

528 wild-type NSC line derived from E13.5 forebrain, and the selected NSCs were maintained in
529 puromycin-containing medium for three passages before puromycin withdrawal.

530 **RT-qPCR**

531 *Prdm16_Expressing*, wild-type and mutant NSCs were cultured and treated with or without
532 BMP4 (Sigma). After 48-hour treatment, total RNAs were extracted using TRIzol reagent
533 (Invitrogen). Total RNA was further cleaned with Turbo DNase (Ambion) and used in reverse-
534 transcription with RT master mix (ThermoFisher). To ensure the absence of genomic DNA,
535 control qPCR was performed on the mock-reverse-transcribed RNA samples. The list of qPCR
536 primers is included in supplementary table 1.

537 **SCRINSHOT**

538 Brain sections were prepared in the same way as for regular *in situ* hybridization (described
539 above). The SCRINSHOT experiments were carried out according to the published method
540 (Sountoulidis et al., 2020). In brief, 3 padlock probes and 3 corresponding detection probes
541 were designed for each gene of interest. The slides with cryo-sectioned brain slices were
542 pretreated at 45˚C to reduce moisture and fixed in 4% PFA in 1X PBS, followed by washing in
543 PBS Tween-20 0.05% twice. Permeabilization of tissues were done by washing slides in 0.1M
544 HCl for 2mins 15s, followed by washing in PBS Tween-20 0.05% twice. Then a stepwise
545 dehydration was performed for the slides in 70%, 85% & 100% Ethanol and air. The SecureSeal
546 hybridization chamber (GRACE BIO-LABS, 621501) was then mounted to cover each pair of
547 control and *Prdm16* mutant brain slices. Samples were then blocked in a probe-free
548 hybridization reaction mixture of 1XAmplifase buffer (Lucigen, A1905B), 0.05M KCl, 20%
549 Formamide deionized (Millipore S4117), 0.1uM Oligo-dT, 0.1ug/ul BSA (New England
550 Biolabs, B9000S), 1U/ul RiboLock (Thermo, EO0384), and 0.2ug/ul tRNAs (Ambion,
551 AM7119). Then hybridization of padlock probes was done by incubating samples with padlock
552 probes (with the concentration of each one 0.01uM) mixed in blocking reagents used before
553 (no oligo dT used in this step). The slide was then put into a PCR machine to denature at 55˚C
554 for 15 minutes and hybridize at 45˚C for 120 minutes. Padlock probes were then ligated by
555 using SplintR ligase (NEB M0375) at 25˚C for 16 hours followed by RCA (rolling cycle
556 amplification) at 30˚C for 16 hours by using phi29 polymerase (Lucigen, 30221–2) and RCA
557 primer1. Then a fixation step was applied to stabilize RCA product in 4% PFA for 15 minutes
558 followed by washing in PBS Tween-20 0.05%. Then the hybridization of the first 3 genes was

559 done by mixing all 3 3' fluorophore-conjugated detection probes of each gene in reaction
560 reagent (2XSSC, 20% Formamide deionized, 0.1ug/ul BSA, and 0.5 ng/µl DAPI (Biolegend,
561 422801) followed by hybridization at 30˚C for 1 hour. The slides were washed in 20%
562 formamide in 2X SSC and then in 6X SSC, followed by dehydration in 70%, 85%, 100%
563 Ethanol until the chamber was removed. Then the samples were preserved in SlowFade Gold
564 Antifade mountnant (Thermo, S36936) and kept in dark before imaging. After image
565 acquisition, the first 3 detection probes were removed by using Uracil-DNA Glycosylase
566 (Thermo, EN0362), and the slides were ready for the next round of detection probe
567 hybridization. The procedure was repeated until all genes were hybridized and imaged.

568 Images were acquired with Zeiss Axio Observer 7 fluorescent microscope with an automated
569 stage setting to fix imaging region for different hybridization rounds. Image analysis was done
570 according to the published method (Sountoulidis et al., 2020). In brief, the DAPI channel from
571 each round was extracted to measure the shift of imaging. The images were then aligned for all
572 gene channels in Zen by Creating Image Subset with the shifting value. After alignment, images
573 were exported into TIFF files and the threshold analysis was carried out for individual channel
574 one by one in CellProfiler with scripts provided by the published method (Alexandros et al.
575 2020). Then nuclear segmentation was done manually in Fiji ROI manager to obtain nuclear
576 ROIs, followed by an expansion of 2 um in CellProfiler to obtain cell ROIs. Then signal dots
577 were count in these cell ROIs for each gene in CellProfiler and Fiji. Summary of the dot counts
578 for each gene was exported to Excel files.

579 **CUT&TAG**

580 CUT&TAG was performed according to the published method (Kaya-Okur et al., 2019). In
581 brief, *Prdm16*_E and *Prdm16* mutant NSCs were cultured in NeuroCult™ Proliferation Kit
582 (Stem cell technologies, 05702) for 3 days with or without BMP4 at concentration of 25ng/ml
583 medium (Sigma, H4916). Cells on day 3 were then shortly rinsed with 1X PBS and resuspended
584 in 1ml cold NE1 buffer on ice. Nuclei were lightly fixed with 0.1% formaldehyde to 1ml PBS
585 at RT for 2 minutes and neutralized with 75mM Glycine. Nuclei were then washed for 3 times,
586 resuspended in 1mL wash buffer and mixed with 90uL Concanavalin A-coated magnetic beads
587 (Polyscience 86057). The nuclei/beads mix was then blocked with 800 uL cold Antibody buffer
588 for 5 minutes and resuspended in 1.2 mL Antibody buffer and aliquoted into 8 tubes with 150
589 uL each. 2 uL Anti-PRDM16 (Generous gift from Bryan Bjork lab) or IgG (SIGMA-ALDRICH,
590 I5006) was added into each tube for an overnight incubation at 4°C. The beads/nuclei/antibody

591 mix was then washed with Dig-wash buffer and incubated with secondary antibody (1:100
592 dilution) for 1 hour. After further washes with the Dig-wash buffer. a pA-Tn5 adaptor complex
593 in Dig-300 buffer was added to the beads for 1 hour reaction. The beads were then washed with
594 Dig-300 buffer before the incubation with 300ul Tagmentation buffer at 37°C for 1 hour. Then
595 10ul 0.5M EDTA, 3uL 10% SDS and 2.5uL 20 mg/mL proteinase K (Invitrogen) were used to
596 stop the reaction. Then the resultant DNA was purified with DNA clean & Concentrator kit
597 (ZYMO Research D4013) and eluted in 25uL Elution buffer. To generate libraries, 21uL
598 fragment DNA was mixed with 2uL 10uM Universal i5 primer, 2uL 10uM uniquely barcoded
599 i7 primer and 25uL PCR master mix (NEB Phusion® High-Fidelity PCR Master Mix with HF
600 Buffer, M0531). The PCR condition was as follows: 72°C 5min, 98°C 30s, repeat 12 times
601 (98°C 10s, 63°C 10s), 72°C 1 min and hold 4°C. The libraries were cleaned with standard
602 Ampure XP beads as previously described. Libraries from four biological replicates were
603 produced for each condition.

604 **ChIP**

605 ChIP was performed as previously described (Dai et al., 2013b). For each ChIP reaction, 10
606 million Prdm16_E, Prdm16_KO NSCs with or without 3-day BMP4 treatment were fixed,
607 lysed and made into chromatin extract. 2ug SMAD4 (Proteintech, 10231-1-AP), 2ug
608 pSMAD1/5/8 (Millipore, AB3848-1), 2ug SMAD3 (abcam, ab227223) and 2 ug c-FOS
609 antibodies (Invitrogen, MA5-15055) were used in each ChIP reaction. The same chromatin
610 lysate was used for sequential ChIP but with more antibodies in each reaction: 5 ug of IgG or
611 the PRDM16 antibody in the first round of immunoprecipitation. The elutes were then
612 precleared again using gamma-bind G beads, divided into two equal halves and
613 immunoprecipitated with 2 ug of IgG or the SMAD4 antibody. The precipitated DNA was
614 reverse cross-linked, and then purified using the Qiagen PCR purification kit.

615 **Computation analyses**

616 **ChIP-seq libraries and analyses.** 0.2% input and ChIPed DNA were made into libraries using
617 the NEBNext Ultra™ II DNA Library Prep Kit and sequenced on the Illumina Nextseq500
618 platform. Three replicates of ChIP-seq samples, after the adaptor trimming by Trimmomatic,
619 were mapped to the UCSC *Mus musculus* (mm10) genome assembly using Bowtie2 with the
620 default parameters. The uniquely mapped reads (with mapping quality >= 20) were used for
621 further analyses. The peaks were called by HOMER (v4.10) (Heinz et al., 2010). The

622 reproducibility between replicates was estimated by Irreproducibility Discovery Rate (IDR),
623 using the HOMER IDR pipeline (https://github.com/karmel/homer-idr). As suggested by the
624 Encode IDR guideline, we used a relatively relaxed parameter "-F 2 -fdr 0.3 -P .1 -L 3 -LP .1"
625 for the true/pseudo/pooled replicates by the HOMER peak calling. The final confident peaks
626 were determined by an IDR < 5%. The peaks that were overlapped with mm10 blacklist were
627 also removed.

628 **CUT&TAG analyses.** The CUT&TAG samples of Prdm16_E and Prdm16 mutant NSCs in
629 four replicates, and of Prdm16 from CH and ChP area at stage 12.5 embryos in three replicates,
630 were mapped to mm10 genome assembly using Bowtie2 (bowtie2 --end-to-end --very-sensitive
631 --no-mixed --no-discordant --phred33 -I 10 -X 700). The CUT&TAG coverage for these
632 samples were generated by bedtools genomeCoverageBed and normalized to the library depths
633 to give a read per million per base (RPM). By using the peak caller SEACR (Meers et al., 2019),
634 which was designed for calling peaks from sparse chromatin profiling data such as CUT&TAG
635 [22], we performed peak calling with FDR < 10% for each replicated sample (SEACR_1.3.sh
636 normalized_coverage 0.1 non stringent output_peaks). To identify confident peaks, we selected
637 the common peaks, which were called from all replicates for each condition. Peak overlapping
638 analysis was performed by Homer mergePeaks function with default parameters. *De novo* motif
639 discovery from SMAD4 and pSMAD1/5/8 peaks in Prdm16_E NSCs and Prdm16 mutant NSCs
640 were performed by MEME-ChIP software (Machanick and Bailey, 2011) (parameters: -ccut
641 100 -meme-p 5 -dna -meme-mod anr -minw 5 -maxw 15 -filter-thresh 0.05).

642 The CUT&TAG samples of H3K4me3 BMP4-treated and non-treated Prdm16_E and
643 Prdm16_KO cells in 2 or 3 replicates were mapped to mm10 genome assembly using Bowtie2
644 (bowtie2 --end-to-end --very-sensitive --no-mixed --no-discordant --phred33 -I 10 -X 700).
645 Differential analysis of TSS up-stream and down-stream 500 bp between Prdm16_E BMP-
646 treated vs non-BMP-treated and Prdm16_KO vs Prdm16_E BMP-treated were performed by
647 Limma R package (Ritchie et al., 2015). Gene Ontology (GO) enrichment analysis of up-
648 regulated and down-regulated regions was performed by PANTHER (Thomas et al., 2022).

649 **scRNA-seq analyses.** The scRNA-seq data of the developing mouse brain were obtained from
650 (La Manno et al., 2021). The counts per cell were normalized by logNormCounts function in
651 Bioconductor package "scater" and the normalized expression data per cell were used to
652 generate gene expression violin plots. To test whether Prdm16 target gene sets of Prdm16 with
653 and without BMP4 and ChP E12.5 are significantly enriched among the scRNA-seq gene mean

expression in each identified cell type cluster, the gene set enrichment analysis (GESA) "fgesa" Bioconductor package was used [ref: Korotkevich G. et al. Fast gene set enrichment analysis. bioRxiv, 2021. http://biorxiv.org/content/early/2016/06/20/060012].

Acknowledgements

We thank the animal experimental core facility and the imaging facility of Stockholm University and Bioinformatics and Expression analysis core facility at Karolinska Institute, Sweden, for their service and support. We thank Christos Samakovlis and his lab members for technical help on SCRINSHOT experiments. We also appreciate technical help from Adrian Martinez Martin, financial support by the Australian Research Council (ARC) Future Fellowship (FT160100143) and ANU Future Scheme to J. W. The project was supported by the research project grant from Swedish Research Council (Vetenskapsrådet, 2020-03543) and the research grants from Swedish Cancerfonden (CAN 2017/529 and 20 1046 PjF 01 H) to Q.D.

Author contributions

Q.D. conceived and designed the project. L.H. performed all of the experiments. J.W performed all computational analysis. Q.D., J.W. and L.H. analysed and interpreted the data. Q.D. wrote the manuscript with input from L.H. and J.W.

679 **Reference:**

680 Aguilo, F., Avagyan, S., Labar, A., Sevilla, A., Lee, D.F., Kumar, P., Lemischka, I.R., Zhou, B.Y.,
681 and Snoeck, H.W. (2011). Prdm16 is a physiologic regulator of hematopoietic stem cells.
682 Blood *117*, 5057-5066.
683 al, A.P.e. (2020). Canonical Wnt signaling exerts bidirectional control on choroid plexus
684 epithelial development. BIORXIV.
685 Arndt, A.K., Schafer, S., Drenckhahn, J.D., Sabeh, M.K., Plovie, E.R., Caliebe, A., Klopocki, E.,
686 Musso, G., Werdich, A.A., Kalwa, H.*, et al.* (2013). Fine mapping of the 1p36 deletion
687 syndrome identifies mutation of PRDM16 as a cause of cardiomyopathy. Am J Hum Genet
688 *93*, 67-77.
689 Baizabal, J.M., Mistry, M., Garcia, M.T., Gomez, N., Olukoya, O., Tran, D., Johnson, M.B.,
690 Walsh, C.A., and Harwell, C.C. (2018). The Epigenetic State of PRDM16-Regulated Enhancers
691 in Radial Glia Controls Cortical Neuron Position. Neuron *98*, 945-962 e948.
692 Benayoun, B.A., Pollina, E.A., Ucar, D., Mahmoudi, S., Karra, K., Wong, E.D., Devarajan, K.,
693 Daugherty, A.C., Kundaje, A.B., Mancini, E.*, et al.* (2014). H3K4me3 breadth is linked to cell
694 identity and transcriptional consistency. Cell *158*, 673-688.
695 Bjork, B.C., Turbe-Doan, A., Prysak, M., Herron, B.J., and Beier, D.R. (2010). Prdm16 is
696 required for normal palatogenesis in mice. Hum Mol Genet *19*, 774-789.
697 Chui, A., Zhang, Q., Dai, Q., and Shi, S.H. (2020). Oxidative stress regulates progenitor
698 behavior and cortical neurogenesis. Development *147*.
699 Chuikov, S., Levi, B.P., Smith, M.L., and Morrison, S.J. (2010). Prdm16 promotes stem cell
700 maintenance in multiple tissues, partly by regulating oxidative stress. Nat Cell Biol *12*, 999-
701 1006.
702 Dai, Q., Andreu-Agullo, C., Insolera, R., Wong, L.C., Shi, S.H., and Lai, E.C. (2013a). BEND6 is a
703 nuclear antagonist of Notch signaling during self-renewal of neural stem cells. Development
704 *140*, 1892-1902.
705 Dai, Q., Ren, A., Westholm, J.O., Serganov, A.A., Patel, D.J., and Lai, E.C. (2013b). The BEN
706 domain is a novel sequence-specific DNA-binding domain conserved in neural transcriptional
707 repressors. Genes Dev *27*, 602-614.
708 Dennler, S., Itoh, S., Vivien, D., ten Dijke, P., Huet, S., and Gauthier, J.M. (1998). Direct
709 binding of Smad3 and Smad4 to critical TGF beta-inducible elements in the promoter of
710 human plasminogen activator inhibitor-type 1 gene. The EMBO journal *17*, 3091-3100.
711 Gao, S., Steffen, J., and Laughon, A. (2005). Dpp-responsive silencers are bound by a trimeric
712 Mad-Medea complex. J Biol Chem *280*, 36158-36164.
713 Geetha-Loganathan, P., Nimmagadda, S., and Scaal, M. (2008). Wnt signaling in limb
714 organogenesis. Organogenesis *4*, 109-115.
715 Gessert, S., and Kuhl, M. (2010). The multiple phases and faces of wnt signaling during
716 cardiac differentiation and development. Circ Res *107*, 186-199.
717 Harrison-Uy, S.J., and Pleasure, S.J. (2012). Wnt signaling and forebrain development. Cold
718 Spring Harb Perspect Biol *4*, a008094.
719 He, L., Jones, J., He, W., Bjork, B.C., Wen, J., and Dai, Q. (2021). PRDM16 regulates a
720 temporal transcriptional program to promote progression of cortical neural progenitors.
721 Development *148*.
722 He, X.C., Zhang, J., Tong, W.G., Tawfik, O., Ross, J., Scoville, D.H., Tian, Q., Zeng, X., He, X.,
723 Wiedemann, L.M.*, et al.* (2004). BMP signaling inhibits intestinal stem cell self-renewal
724 through suppression of Wnt-beta-catenin signaling. Nat Genet *36*, 1117-1121.

725 Hebert, J.M., Mishina, Y., and McConnell, S.K. (2002). BMP signaling is required locally to
726 pattern the dorsal telencephalic midline. Neuron *35*, 1029-1041.
727 Heinz, S., Benner, C., Spann, N., Bertolino, E., Lin, Y.C., Laslo, P., Cheng, J.X., Murre, C., Singh,
728 H., and Glass, C.K. (2010). Simple combinations of lineage-determining transcription factors
729 prime cis-regulatory elements required for macrophage and B cell identities. Mol Cell *38*,
730 576-589.
731 Hill, C.S. (2016). Transcriptional Control by the SMADs. Cold Spring Harb Perspect Biol *8*.
732 Horvath, C., and Scheele, C. (2022). PRDM16 stability and metabolically healthy adipose
733 tissue. Nat Metab *4*, 1095-1096.
734 Inoue, M., Iwai, R., Tabata, H., Konno, D., Komabayashi-Suzuki, M., Watanabe, C., Iwanari,
735 H., Mochizuki, Y., Hamakubo, T., Matsuzaki, F.*, et al.* (2017). Prdm16 is crucial for
736 progression of the multipolar phase during neural differentiation of the developing
737 neocortex. Development *144*, 385-399.
738 Itasaki, N., and Hoppler, S. (2010). Crosstalk between Wnt and bone morphogenic protein
739 signaling: a turbulent relationship. Dev Dyn *239*, 16-33.
740 Johansson, P.A. (2014). The choroid plexuses and their impact on developmental
741 neurogenesis. Front Neurosci *8*, 340.
742 Kajimura, S., Seale, P., Tomaru, T., Erdjument-Bromage, H., Cooper, M.P., Ruas, J.L., Chin, S.,
743 Tempst, P., Lazar, M.A., and Spiegelman, B.M. (2008). Regulation of the brown and white fat
744 gene programs through a PRDM16/CtBP transcriptional complex. Genes Dev *22*, 1397-1409.
745 Kalani, M.Y., Cheshier, S.H., Cord, B.J., Bababeygy, S.R., Vogel, H., Weissman, I.L., Palmer,
746 T.D., and Nusse, R. (2008). Wnt-mediated self-renewal of neural stem/progenitor cells. Proc
747 Natl Acad Sci U S A *105*, 16970-16975.
748 Katada, S., Takouda, J., Nakagawa, T., Honda, M., Igarashi, K., Imamura, T., Ohkawa, Y., Sato,
749 S., Kurumizaka, H., and Nakashima, K. (2021). Neural stem/precursor cells dynamically
750 change their epigenetic landscape to differentially respond to BMP signaling for fate
751 switching during brain development. Genes Dev *35*, 1431-1444.
752 Kaya-Okur, H.S., Wu, S.J., Codomo, C.A., Pledger, E.S., Bryson, T.D., Henikoff, J.G., Ahmad, K.,
753 and Henikoff, S. (2019). CUT&Tag for efficient epigenomic profiling of small samples and
754 single cells. Nat Commun *10*, 1930.
755 Korinek, V., Barker, N., Moerer, P., van Donselaar, E., Huls, G., Peters, P.J., and Clevers, H.
756 (1998). Depletion of epithelial stem-cell compartments in the small intestine of mice lacking
757 Tcf-4. Nat Genet *19*, 379-383.
758 La Manno, G., Siletti, K., Furlan, A., Gyllborg, D., Vinsland, E., Mossi Albiach, A., Mattsson
759 Langseth, C., Khven, I., Lederer, A.R., Dratva, L.M.*, et al.* (2021). Molecular architecture of
760 the developing mouse brain. Nature *596*, 92-96.
761 Lehtinen, M.K., Bjornsson, C.S., Dymecki, S.M., Gilbertson, R.J., Holtzman, D.M., and Monuki,
762 E.S. (2013). The choroid plexus and cerebrospinal fluid: emerging roles in development,
763 disease, and therapy. J Neurosci *33*, 17553-17559.
764 Liddelow, S.A., Dziegielewska, K.M., Vandeberg, J.L., and Saunders, N.R. (2010).
765 Development of the lateral ventricular choroid plexus in a marsupial, Monodelphis
766 domestica. Cerebrospinal Fluid Res *7*, 16.
767 Lun, M.P., Monuki, E.S., and Lehtinen, M.K. (2015). Development and functions of the
768 choroid plexus-cerebrospinal fluid system. Nat Rev Neurosci *16*, 445-457.
769 Machanick, P., and Bailey, T.L. (2011). MEME-ChIP: motif analysis of large DNA datasets.
770 Bioinformatics *27*, 1696-1697.

771 Meers, M.P., Tenenbaum, D., and Henikoff, S. (2019). Peak calling by Sparse Enrichment
772 Analysis for CUT&RUN chromatin profiling. Epigenetics Chromatin *12*, 42.
773 Mira, H., Andreu, Z., Suh, H., Lie, D.C., Jessberger, S., Consiglio, A., San Emeterio, J.,
774 Hortiguela, R., Marques-Torrejon, M.A., Nakashima, K.*, et al.* (2010). Signaling through
775 BMPR-IA regulates quiescence and long-term activity of neural stem cells in the adult
776 hippocampus. Cell stem cell *7*, 78-89.
777 Nie, X., Luukko, K., and Kettunen, P. (2006). BMP signalling in craniofacial development. Int J
778 Dev Biol *50*, 511-521.
779 Parichha, A., Suresh, V., Chatterjee, M., Kshirsagar, A., Ben-Reuven, L., Olender, T., Taketo,
780 M.M., Radosevic, V., Bobic-Rasonja, M., Trnski, S.*, et al.* (2022). Constitutive activation of
781 canonical Wnt signaling disrupts choroid plexus epithelial fate. Nat Commun *13*, 633.
782 Pellegrini, L., Bonfio, C., Chadwick, J., Begum, F., Skehel, M., and Lancaster, M.A. (2020).
783 Human CNS barrier-forming organoids with cerebrospinal fluid production. Science *369*.
784 Pliner, H.A., Packer, J.S., McFaline-Figueroa, J.L., Cusanovich, D.A., Daza, R.M., Aghamirzaie,
785 D., Srivatsan, S., Qiu, X., Jackson, D., Minkina, A.*, et al.* (2018). Cicero Predicts cis-Regulatory
786 DNA Interactions from Single-Cell Chromatin Accessibility Data. Mol Cell *71*, 858-871 e858.
787 Pyrowolakis, G., Hartmann, B., Muller, B., Basler, K., and Affolter, M. (2004). A simple
788 molecular complex mediates widespread BMP-induced repression during Drosophila
789 development. Dev Cell *7*, 229-240.
790 Rhodes, C.T., Thompson, J.J., Mitra, A., Asokumar, D., Lee, D.R., Lee, D.J., Zhang, Y., Jason, E.,
791 Dale, R.K., Rocha, P.P.*, et al.* (2022). An epigenome atlas of neural progenitors within the
792 embryonic mouse forebrain. Nat Commun *13*, 4196.
793 Ritchie, M.E., Phipson, B., Wu, D., Hu, Y., Law, C.W., Shi, W., and Smyth, G.K. (2015). limma
794 powers differential expression analyses for RNA-sequencing and microarray studies. Nucleic
795 Acids Res *43*, e47.
796 Robert, B. (2007). Bone morphogenetic protein signaling in limb outgrowth and patterning.
797 Dev Growth Differ *49*, 455-468.
798 Shimada, I.S., Acar, M., Burgess, R.J., Zhao, Z., and Morrison, S.J. (2017). Prdm16 is required
799 for the maintenance of neural stem cells in the postnatal forebrain and their differentiation
800 into ependymal cells. Genes Dev *31*, 1134-1146.
801 Shull, L.C., Lencer, E.S., Kim, H.M., Goyama, S., Kurokawa, M., Costello, J.C., Jones, K., and
802 Artinger, K.B. (2022). PRDM paralogs antagonistically balance Wnt/beta-catenin activity
803 during craniofacial chondrocyte differentiation. Development *149*.
804 Sountoulidis, A., Liontos, A., Nguyen, H.P., Firsova, A.B., Fysikopoulos, A., Qian, X., Seeger,
805 W., Sundstrom, E., Nilsson, M., and Samakovlis, C. (2020). SCRINSHOT enables spatial
806 mapping of cell states in tissue sections with single-cell resolution. PLoS Biol *18*, e3000675.
807 Stine, R.R., Sakers, A.P., TeSlaa, T., Kissig, M., Stine, Z.E., Kwon, C.W., Cheng, L., Lim, H.W.,
808 Kaestner, K.H., Rabinowitz, J.D.*, et al.* (2019). PRDM16 Maintains Homeostasis of the
809 Intestinal Epithelium by Controlling Region-Specific Metabolism. Cell stem cell *25*, 830-845
810 e838.
811 Strassman, A., Schnutgen, F., Dai, Q., Jones, J.C., Gomez, A.C., Pitstick, L., Holton, N.E.,
812 Moskal, R., Leslie, E.R., von Melchner, H.*, et al.* (2017). Generation of a multipurpose Prdm16
813 mouse allele by targeted gene trapping. Dis Model Mech *10*, 909-922.
814 Takahata, M., Inoue, Y., Tsuda, H., Imoto, I., Koinuma, D., Hayashi, M., Ichikura, T., Yamori,
815 T., Nagasaki, K., Yoshida, M.*, et al.* (2009). SKI and MEL1 cooperate to inhibit transforming
816 growth factor-beta signal in gastric cancer cells. J Biol Chem *284*, 3334-3344.

817 Thomas, P.D., Ebert, D., Muruganujan, A., Mushayahama, T., Albou, L.P., and Mi, H. (2022).
818 PANTHER: Making genome-scale phylogenetics accessible to all. Protein Sci *31*, 8-22.
819 van Wijk, B., Moorman, A.F., and van den Hoff, M.J. (2007). Role of bone morphogenetic
820 proteins in cardiac differentiation. Cardiovasc Res *74*, 244-255.
821 Wang, Q., Li, H., Tajima, K., Verkerke, A.R.P., Taxin, Z.H., Hou, Z., Cole, J.B., Li, F., Wong, J.,
822 Abe, I.*, et al.* (2022). Post-translational control of beige fat biogenesis by PRDM16
823 stabilization. Nature *609*, 151-158.
824 Warner, D.R., Horn, K.H., Mudd, L., Webb, C.L., Greene, R.M., and Pisano, M.M. (2007).
825 PRDM16/MEL1: a novel Smad binding protein expressed in murine embryonic orofacial
826 tissue. Biochim Biophys Acta *1773*, 814-820.
827 Watanabe, M., Kang, Y.J., Davies, L.M., Meghpara, S., Lau, K., Chung, C.Y., Kathiriya, J.,
828 Hadjantonakis, A.K., and Monuki, E.S. (2012). BMP4 sufficiency to induce choroid plexus
829 epithelial fate from embryonic stem cell-derived neuroepithelial progenitors. J Neurosci *32*,
830 15934-15945.
831 Weiss, A., Charbonnier, E., Ellertsdottir, E., Tsirigos, A., Wolf, C., Schuh, R., Pyrowolakis, G.,
832 and Affolter, M. (2010). A conserved activation element in BMP signaling during Drosophila
833 development. Nat Struct Mol Biol *17*, 69-76.
834 Wolff, J.E., Sajedi, M., Brant, R., Coppes, M.J., and Egeler, R.M. (2002). Choroid plexus
835 tumours. British journal of cancer *87*, 1086-1091.
836 Wong, C., Rougier-Chapman, E.M., Frederick, J.P., Datto, M.B., Liberati, N.T., Li, J.M., and
837 Wang, X.F. (1999). Smad3-Smad4 and AP-1 complexes synergize in transcriptional activation
838 of the c-Jun promoter by transforming growth factor beta. Mol Cell Biol *19*, 1821-1830.
839 Zawel, L., Dai, J.L., Buckhaults, P., Zhou, S., Kinzler, K.W., Vogelstein, B., and Kern, S.E. (1998).
840 Human Smad3 and Smad4 are sequence-specific transcription activators. Mol Cell *1*, 611-
841 617.
842 Zhang, J., and Li, L. (2005). BMP signaling and stem cell regulation. Developmental biology
843 *284*, 1-11.
844 Zhang, Y., Feng, X.H., and Derynck, R. (1998). Smad3 and Smad4 cooperate with c-Jun/c-Fos
845 to mediate TGF-beta-induced transcription. Nature *394*, 909-913.
846
847
848
849
850
851
852
853
854
855
856
857

858 **Figure legend**

859 *Figure 1. Prdm16 mutant ChP cells fail to exit cell cycle and are still neural progenitors*

860 (**A**) RNA *in situ* hybridization with a *Prdm16* probe, showing expression of *Prdm16* in the
861 E10.5 and E12.5 brains. The line and bracket indicate the developing ChP. (**B**) Staining of
862 PRDM16 using a PRDM16 antibody on the E13.5 control and null mutant brains. Red:
863 PRDM16; blue: the nucleus dye DAPI. White arrows indicate the ChP in the control. (**C-D**)
864 RNA in situ hybridization using a *Ttr* probe on E12.5 control and *Prdm16* null mutant brains.
865 Brain sections with tChP and hChP areas are shown separately. (**E**) Two-hour EdU labeling in
866 the E12.5 control and homozygous brains. The brain sections are co-stained with an antibody
867 against B-gal. Note: the lacZ gene trap is present in the heterozygous and homozygous mutants
868 but not in wild-type animals, and the highest expression of B-Gal is seen at the ChP indicated
869 by brackets. Red: B-Gal; blue: the nucleus dye DAPI; green: EdU. (**F**) DCX antibody staining
870 on the E12.5 control and homozygous brain slices. White arrows indicate some of the DCX
871 positive cells. Quantification of EdU+ (**E**) or DCX+ (**F**) cells is shown on the right. Biological
872 replicates: N=3. Error bars represent standard deviation (SD). Statistical significance is
873 calculated using unpaired t-test. ***, $p<0.001$.

874 *Figure 2. Prdm16 is required for BMP4-induced NSC quiescence*

875 (**A**) Illustration of the NSC culture assay. (**B**) Immunostaining of mKI67 in red and SOX2 in
876 green and EdU labeling in blue on indicated NSC genotypes and treatment. (**C**) Quantification
877 of the fraction of mKI67+ or EdU+ cells among the total cell number marked by SOX2. (**D**)
878 RT-qPCR measurement of *mKi67* RNA levels relative to 18S RNAs. Biological replicates: N=3.
879 (**E**) Quantification of *Ttr* expression in indicated cell types upon BMP4 treatment. RT-qPCR
880 values of Ttr is first normalized to 18S RNAs and then to that of the wild-type control cells.
881 Error bars represent standard deviation (SD). Statistical significance is calculated using
882 unpaired t-test. ***, $p<0.001$; **, p< 001; *, $p<0.05$; n.s., non-significant.

883

884 *Figure 3. BMP signaling represses cell proliferation genes to induce cell quiescence*

885 (**A**) Heatmaps of ChIP-seq coverage (normalized by library depths and input) centered at peak
886 summits for SMAD4, pSMAD1/5/8 and SMAD3 in *Prdm16_E* cells with or without BMP4.

887 (**B**) A volcano plot of differential H3K4me3 read counts at TSS in *Prdm16_E* cells with BMP4
888 versus those with no BMP4. Significant changes ($P < 0.01$) are colored. (**C**) A bubble plot
889 showing GO terms significantly enriched in SMAD-repressed genes (labelled in dark green in
890 B). (**D**) A volcano plot of differential H3K4me3 read counts at TSS in *Prdm16_KO* cells with
891 BMP4 versus *Prdm16_E* cells with BMP4. Significant changes ($P < 0.01$) are colored. **(E)** A
892 heatmap of H3K4me3 normalized read counts at TSS of the 31 genes co-repressed by PRDM16
893 and SMADs (overlapping genes from those in dark green in B and those in dark pink in D). (**F**)
894 RT-qPCR measurement of *Wnt7b* mRNA levels in indicated genotypes and conditions from
895 three biological replicates, each with two technical replicates. Statistical significance was
896 calculated using unpaired t-test (***, p<0.001; **, p< 0.01; *, p<0.05; n.s., non-significant).
897 (**G**) Genome browser snapshots showing the H3K4me4 CUT&TAG tracks in the *Wnt7b* and
898 *Cdkn1a* loci.

899 *Figure 4. PRDM16 anchors the SMAD proteins at specific genomic regions to mediate*
900 *repression*

901 (**A)** A Venn diagram showing the overlap of CUT&TAG peak in BMP4-treated and non-treated
902 Prdm16_E cells. **(B)** The mean coverages (normalized by library depths) centered at peak
903 summits are shown for the PRDM16 CUT&TAG signal in BMP4-treated and non-treated
904 *Prdm16_E* cells and Prdm16_KO mutant samples (4 replicates combined). **(C)** Metaplots of
905 SMAD4 and pSMAD1/5/8 ChIP-seq coverage centered at SMAD or pSMAD peak summits
906 that have PRDM16 co-binding (top) and those without PRDM16 co-binding (bottom) in BMP4
907 treated *Prdm16_E* and *Prdm16_KO* cells. The average coverage is plotted in the bar plots on
908 the right. Only the peaks with PRDM16 co-binding show significant reduction in the KO cells
909 (*** P<0.001; ** P<0.01; * P<0.05; n.a. P>0.05). **(D-E)** Genome browser view of the *Wnt7b*
910 and *Id1* loci, showing PRDM16 CUT&TAG and SMAD ChIP-seq tracks. The co-bound
911 regions are highlighted. **(F-G)** ChIP-qPCR validation of SMAD4 binding to the highlighted
912 regions in D-E from *Prdm16_E* and *Prdm16_KO* cells with two replicates. (**H**) The occurrence
913 frequency of four types of SMAD motifs is shown in five binned SMAD ChP-seq peaks scored
914 from low to high. The palindromic motif GTCTAGAC shows the highest occurrence frequency
915 in peaks with PRDM16 co-binding (solid red) and is the only one that has reduced occurrence
916 frequency in peaks without PRDM16 co-binding (dashed red).

917 *Figure 5. The SMAD complex switches genome localization in the absence of Prdm16*

918 (**A-B**) Genome browser snapshots of the *Id3* (top) and *Wnt7b* (bottom) gene loci, showing
919 ectopic SMAD peaks, indicated by the arrows. **(C)** The volcano plots showing differential
920 SMAD4 and pSMAD1/5/8 ChIP-seq read counts in BMP4-treated *Prdm16_KO* cells compared
921 to BMP4-treated *Prdm16_E* cells. The sites in blue are co-bound by PRDM16, while the sites
922 in red are not bound by PRDM16 but within the 200kb of a PRDM16-cobound site. The average
923 log2 fold-change is plotted on the right. (**D-E**) *De novo* motif discovery from SMAD4 and
924 pSMAD1/5/8 ChIP-seq peaks in *Prdm16_E* cells (**D**) and *Prdm16_KO* cells (**E**). (**F-G**) ChIP-
925 qPCR validation of increased SMAD4 and c-FOS occupancy at the highlighted ectopic sites in
926 *Prdm16_KO* mutant cells versus *Prdm16_E* cells. The locations of PCR amplicons are shown
927 in A and B. **(H)** An enhancer switch model demonstrating that SMADs change co-factors and
928 become into a transcriptional activator in the absence of PRDM16.

929 *Figure 6. PRDM16 and SMADs co-regulated genes are differentially expressed in the ChP and*
930 *neural cells*

931 (**A**) An illustration of the CH and ChP regions with opposite Wnt and BMP gradients and a
932 violin plot of scRNA-seq gene expression at E12.5 for the indicated genes in several selected
933 cell type clusters reanalyzed from (La Manno et al., 2021). Definition of the clusters is based
934 on marker gene expression from E9.5-E18.5 brain cells. These include the choroid plexus
935 clusters 1-5 (Chpl), with cluster Chpl5 identified by this study based on *Ttr* expression, Radial
936 glia clusters (RglCH 1-3, RglDF 6-10, and RglF7). CH: cortical hem; DF: dorsal forebrain; F:
937 forebrain. Per cell expression was normalized to give a log2 normalized counts. **(B)** Metaplots
938 and heatmaps of PRDM16 and IgG CUT&TAG coverage (normalized by library depths)
939 centered at peak summits from E12.5 dorsal midline tissues. **(C)** A genome browser snapshot
940 of the *Wnt7b* locus, showing PRDM16 CUT&TAG and SMADs ChIP-seq tracks.

941 *Figure 7. PRDM16 suppresses Wnt signaling and cell proliferation in the ChP epithelial cells*
942

943 (**A**) SCRINSHOT images of E11.5 wild-type and *Prdm16* mutant brains, with *BMP4*, *Ttr*,
944 *Wnt7b* and *Wnt2b* probes. Note: The red arrows indicate a strong unspecific signal in all
945 channels due to autofluorescence of blood cells. The cells selected for quantification are shown
946 together with the DAPI channel. (**B**) Enlarged views of SCRINSHOT images at the area
947 indicated in A, showing an increase of Wnt and neural gene expression levels and decrease of
948 *Ttr* and *Prdm16*. (**C**) A violin plot with the dot counts measuring expression levels of the 24
949 genes examined. Each gene is measured in 330 CH and 330 ChP cells from three wild-type and

950 three Prdm16 mutant samples. (**D**) SCRINSHOT images for E12.5 wild-type and Prdm16
951 mutant brains, with Axin2, Ttr, Wnt 7b, Wnt2b and mKi67 probes. (**E**) Enlarged views of the
952 areas indicated in the dash-lined rectangles in D. The ChP parts are highlighted by dashed lines.
953 (**F**) Distribution of dot counts for indicated genes in the wild-type (*wt*) and *Prdm16* mutant (*mut*)
954 CH and ChP areas. The X-axis shows the 110 cells in each replicate, and the Y-axis shows the
955 mean value of the number of counts in three biological replicates. P value was calculated using
956 area under the ROC curve in Prism Graphpad. (**G**) Multi-variant linear regression of *mKi67*,
957 *Axin2* and *Ttr* using the dot counts for each gene in three pairs of wild-type and *Prdm16* mutant
958 samples. All 660 cells including both CH and ChP tissues in each genotype are included.
959 Pearson correlation and statistical difference were calculated in Prism Graphpad. (H)
960 Illustration of the regulatory circuit, which is required for transitioning proliferative NSCs to
961 quiescent NSCs, a prerequisite for the specification of ChP epithelial cells.
962

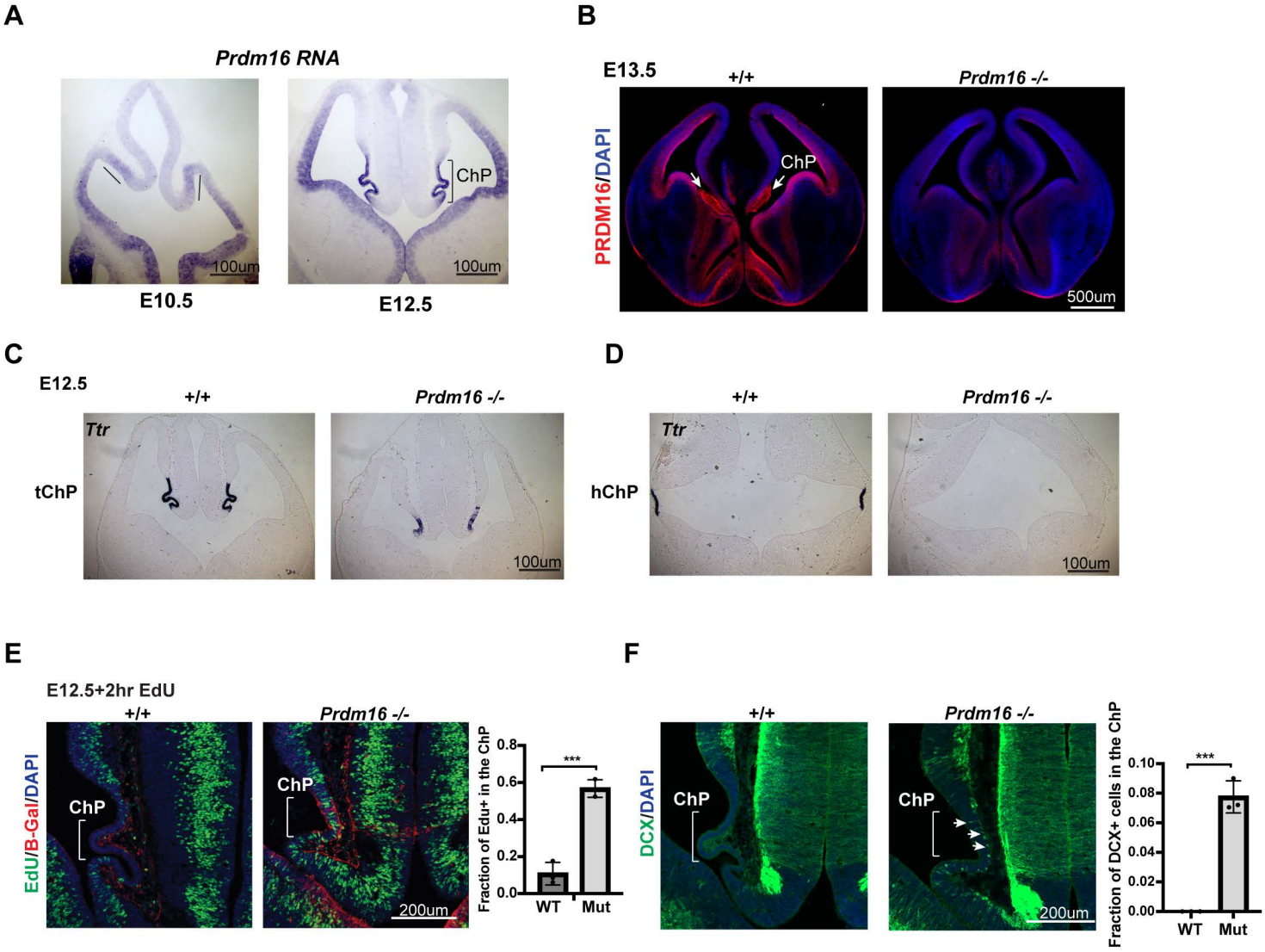
A
Prdm16 RNA
ChP
100um
100um
E10.5
E12.5
B
E13.5
+/+
Prdm16 -/-
PRDM16/DAPI
ChP
500um
C
E12.5
+/+
Prdm16 -/-
Ttr
tChP
100um
D
+/+
Prdm16 -/-
Ttr
hChP
100um
E
E12.5+2hr EdU
+/+
Prdm16 -/-
EdU/B-Gal/DAPI
ChP
ChP
200um
Fraction of Edu+ in the ChP
0.8
0.6
0.4
0.2
0.0
***
WT
Mut
F
+/+
Prdm16 -/-
DCX/DAPI
ChP
ChP
200um
Fraction of DCX+ cells in the ChP
0.10
0.08
0.06
0.04
0.02
0.00
***
WT
Mut

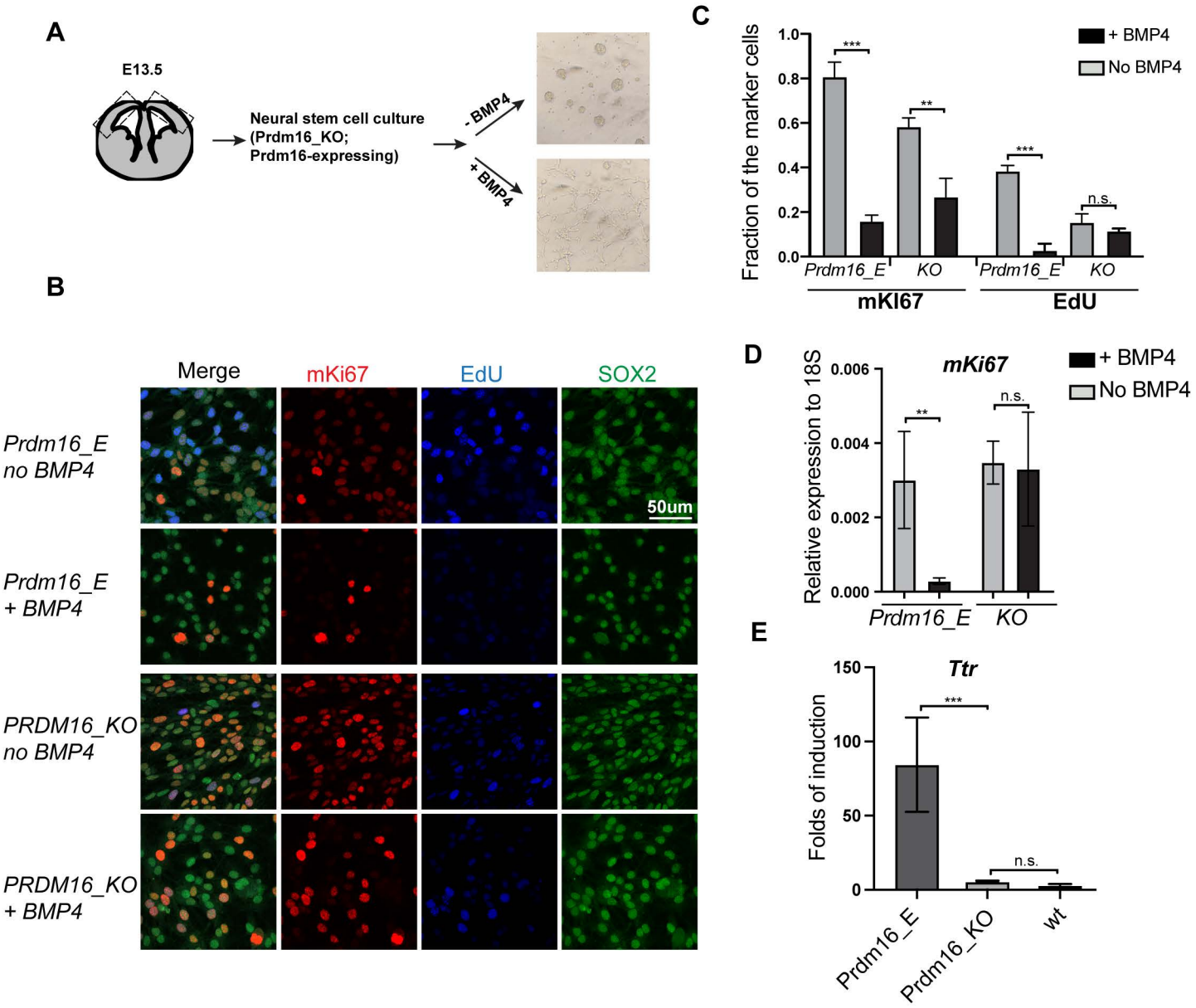
A
E13.5
Neural stem cell culture
(Prdm16_KO;
Prdm16-expressing)
- BMP4
+ BMP4
B
Merge
mKi67
EdU
SOX2
Prdm16_E
no BMP4
Prdm16_E
+ BMP4
PRDM16_KO
no BMP4
PRDM16_KO
+ BMP4
50um
C
Fraction of the marker cells
1.0
0.8
0.6
0.4
0.2
0.0
***
**
***
n.s.
+ BMP4
No BMP4
Prdm16_E
KO
Prdm16_E
KO
mKI67
EdU
D
mKi67
Relative expression to 18S
0.006
0.004
0.002
0.000
**
n.s.
+ BMP4
No BMP4
Prdm16_E
KO
E
Ttr
Folds of induction
150
100
50
0
***
n.s.
Prdm16_E
Prdm16_KO
wt

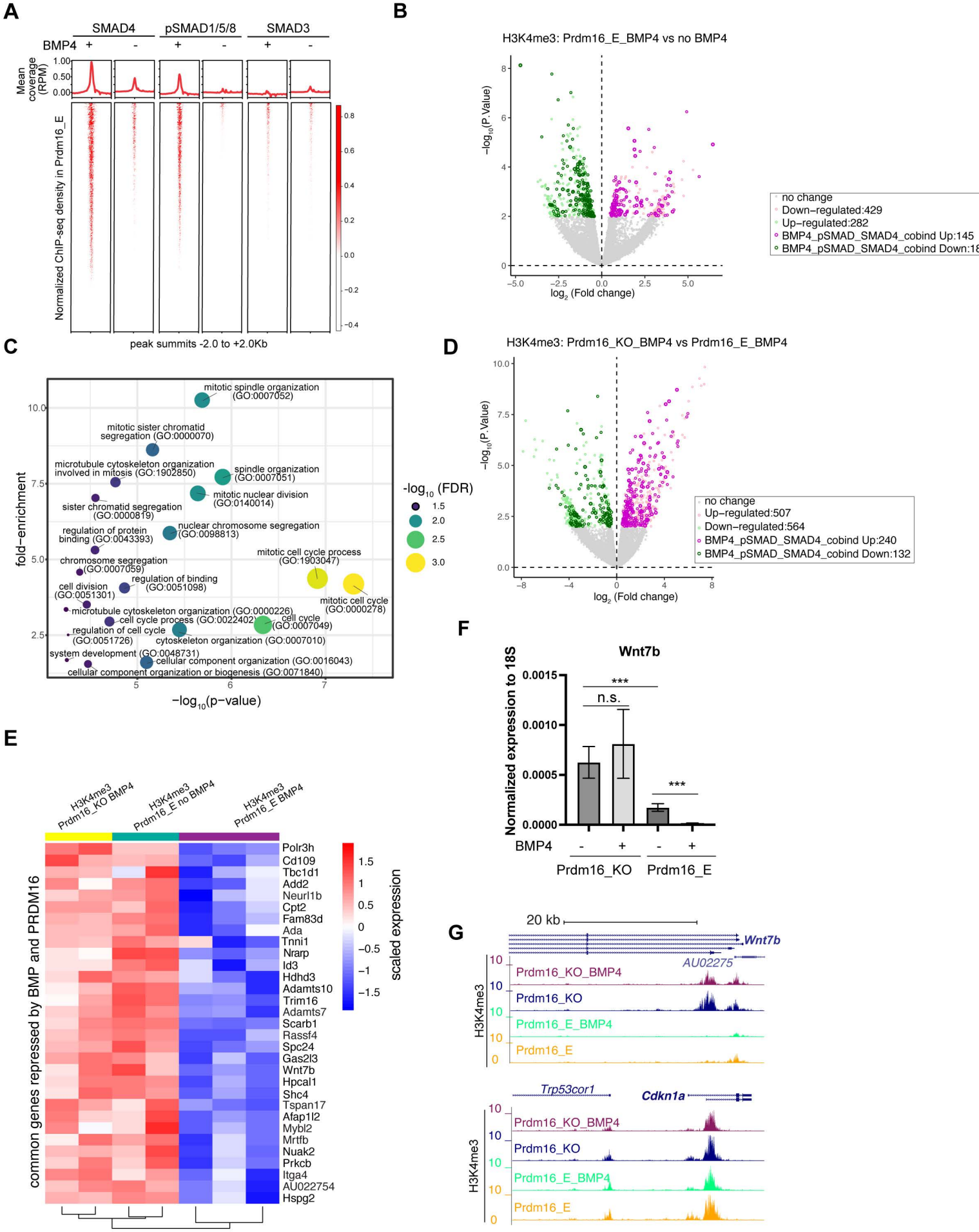
A
SMAD4
pSMAD1/5/8
SMAD3
BMP4 + - + - + -
Mean coverage (RPM)
Normalized ChIP-seq density in Prdm16_E
peak summits -2.0 to +2.0Kb
B
H3K4me3: Prdm16_E_BMP4 vs no BMP4
−log10(P.Value)
log2 (Fold change)
no change
Down−regulated:429
Up−regulated:282
BMP4_pSMAD_SMAD4_cobind Up:145
BMP4_pSMAD_SMAD4_cobind Down:18
C
mitotic spindle organization (GO:0007052)
mitotic sister chromatid segregation (GO:0000070)
microtubule cytoskeleton organization involved in mitosis (GO:1902850)
spindle organization (GO:0007051)
mitotic nuclear division (GO:0140014)
sister chromatid segregation (GO:0000819)
regulation of protein binding (GO:0043393)
nuclear chromosome segregation (GO:0098813)
mitotic cell cycle process (GO:1903047)
chromosome segregation (GO:0007059)
regulation of binding (GO:0051098)
cell division (GO:0051301)
mitotic cell cycle (GO:0000278)
microtubule cytoskeleton organization (GO:0000226)
cell cycle process (GO:0022402)
cell cycle (GO:0007049)
regulation of cell cycle (GO:0051726)
cytoskeleton organization (GO:0007010)
system development (GO:0048731)
cellular component organization (GO:0016043)
cellular component organization or biogenesis (GO:0071840)
fold−enrichment
−log10(p−value)
-log10 (FDR)
1.5
2.0
2.5
3.0
D
H3K4me3: Prdm16_KO_BMP4 vs Prdm16_E_BMP4
−log10(P.Value)
log2 (Fold change)
no change
Up−regulated:507
Down−regulated:564
BMP4_pSMAD_SMAD4_cobind Up:240
BMP4_pSMAD_SMAD4_cobind Down:132
E
H3K4me3 Prdm16_KO BMP4
H3K4me3 Prdm16_E no BMP4
H3K4me3 Prdm16_E BMP4
common genes repressed by BMP and PRDM16
Polr3h
Cd109
Tbc1d1
Add2
Neurl1b
Cpt2
Fam83d
Ada
Tnni1
Nrarp
Id3
Hdhd3
Adamts10
Trim16
Adamts7
Scarb1
Rassf4
Spc24
Gas2l3
Wnt7b
Hpcal1
Shc4
Tspan17
Afap1l2
Mybl2
Mrtfb
Nuak2
Prkcb
Itga4
AU022754
Hspg2
scaled expression
F
Wnt7b
Normalized expression to 18S
***
n.s.
***
BMP4 - + - +
Prdm16_KO
Prdm16_E
G
20 kb
Wnt7b
AU02275
H3K4me3
Prdm16_KO_BMP4
Prdm16_KO
Prdm16_E_BMP4
Prdm16_E
Trp53cor1
Cdkn1a
H3K4me3
Prdm16_KO_BMP4
Prdm16_KO
Prdm16_E_BMP4
Prdm16_E

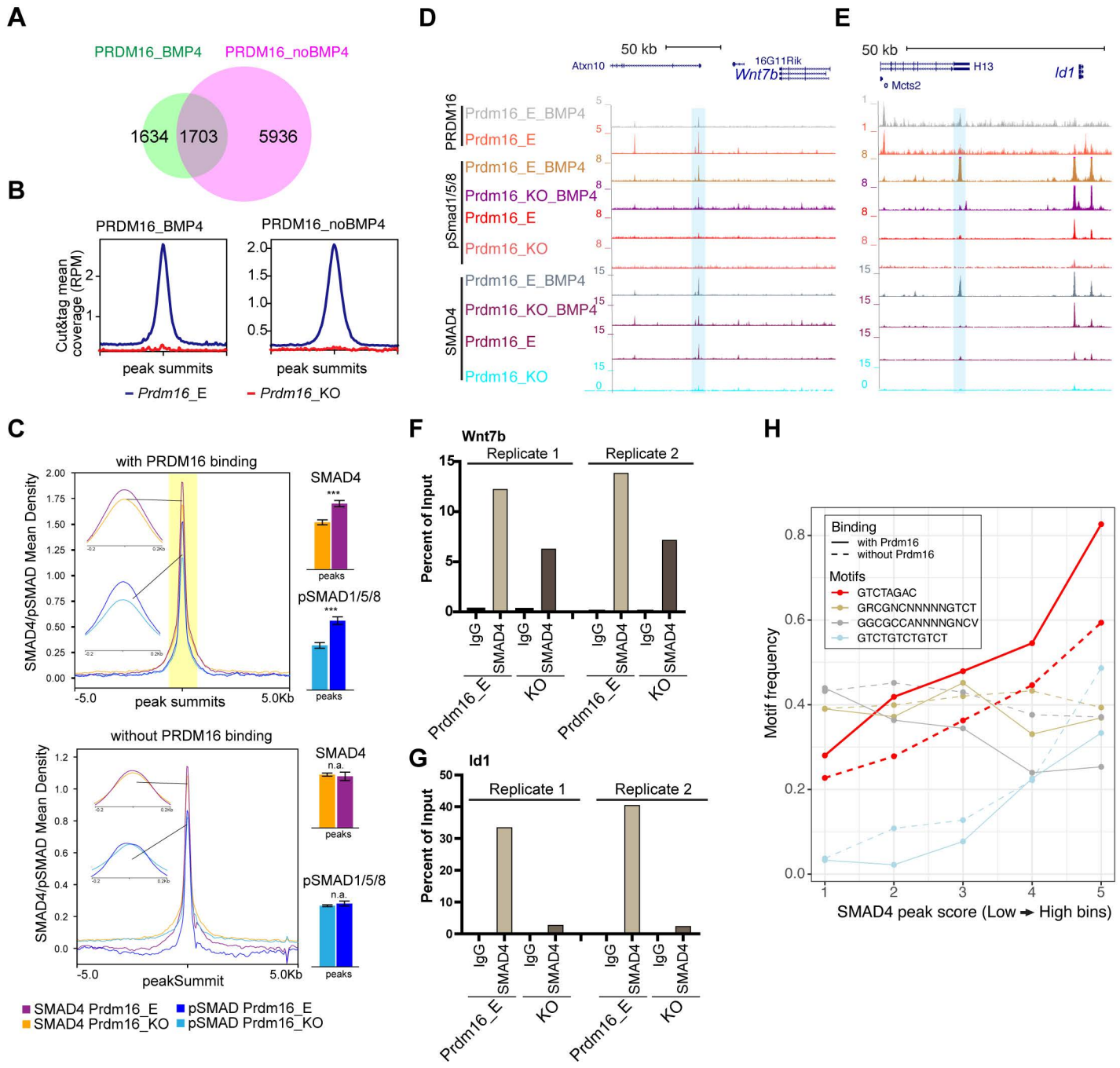
A
PRDM16_BMP4
PRDM16_noBMP4
1634
1703
5936
B
PRDM16_BMP4
PRDM16_noBMP4
Cut&tag mean coverage (RPM)
peak summits
Prdm16_E
Prdm16_KO
C
with PRDM16 binding
SMAD4/pSMAD Mean Density
peak summits
SMAD4
pSMAD1/5/8
peaks
without PRDM16 binding
peakSummit
n.a.
SMAD4 Prdm16_E
SMAD4 Prdm16_KO
pSMAD Prdm16_E
pSMAD Prdm16_KO
D
50 kb
Atxn10
16G11Rik
Wnt7b
PRDM16
pSmad1/5/8
SMAD4
Prdm16_E_BMP4
Prdm16_E
Prdm16_KO_BMP4
Prdm16_KO
E
50 kb
H13
Id1
Mcts2
F
Wnt7b
Replicate 1
Replicate 2
Percent of Input
IgG
SMAD4
Prdm16_E
KO
G
Id1
H
Binding
with Prdm16
without Prdm16
Motifs
GTCTAGAC
GRCGNCNNNNNGTCT
GGCGCCANNNNGNCV
GTCTGTCTGTCT
Motif frequency
SMAD4 peak score (Low → High bins)

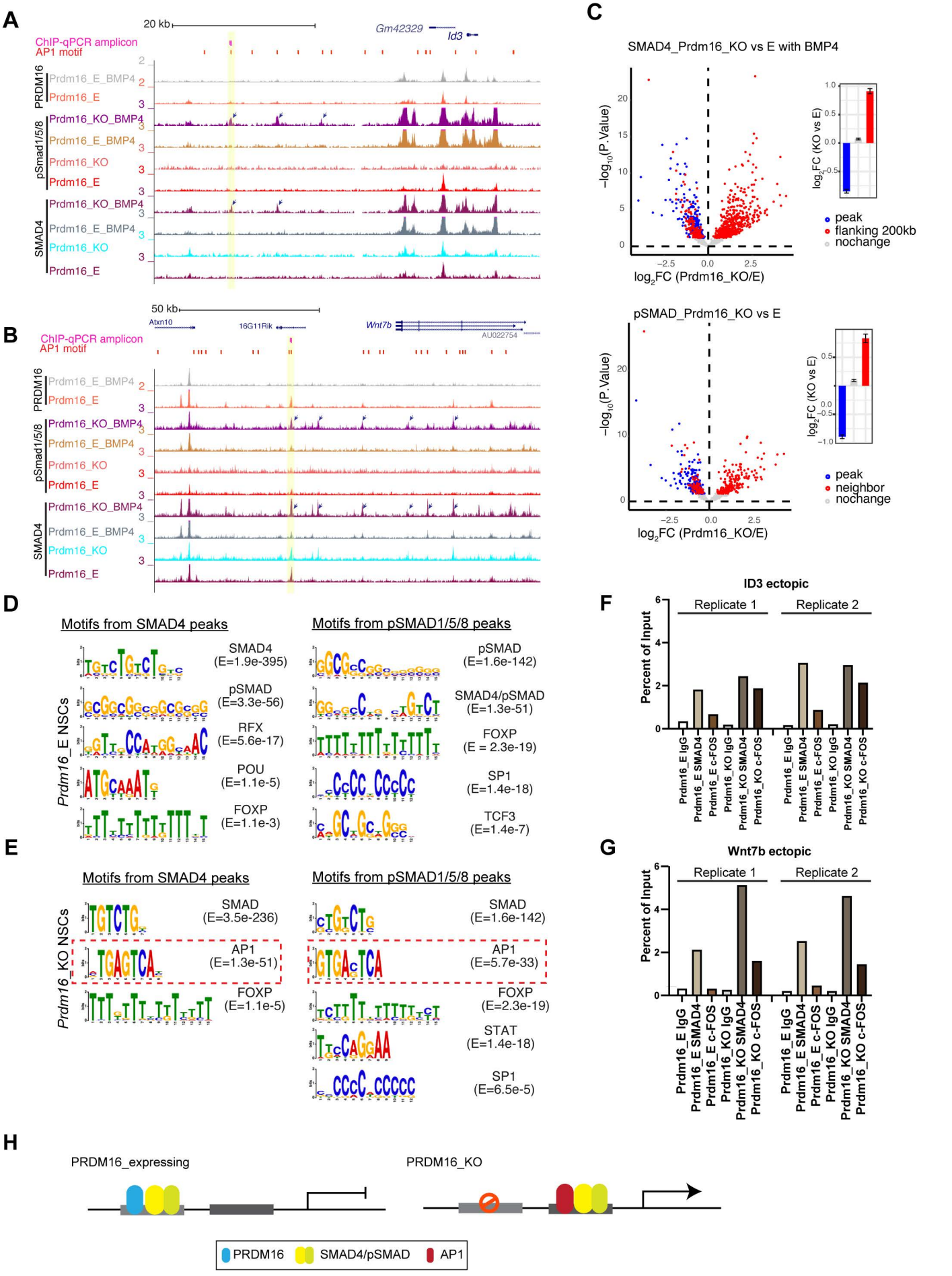
A
20 kb
Gm42329
Id3
ChIP-qPCR amplicon
AP1 motif
PRDM16
Prdm16_E_BMP4
Prdm16_E
pSmad1/5/8
Prdm16_KO_BMP4
Prdm16_E_BMP4
Prdm16_KO
Prdm16_E
SMAD4
Prdm16_KO_BMP4
Prdm16_E_BMP4
Prdm16_KO
Prdm16_E
B
50 kb
Atxn10
16G11Rik
Wnt7b
AU022754
ChIP-qPCR amplicon
AP1 motif
PRDM16
Prdm16_E_BMP4
Prdm16_E
pSmad1/5/8
Prdm16_KO_BMP4
Prdm16_E_BMP4
Prdm16_KO
Prdm16_E
SMAD4
Prdm16_KO_BMP4
Prdm16_E_BMP4
Prdm16_KO
Prdm16_E
C
SMAD4_Prdm16_KO vs E with BMP4
−log10(P.Value)
log2FC (Prdm16_KO/E)
log2FC (KO vs E)
peak
flanking 200kb
nochange
pSMAD_Prdm16_KO vs E
−log10(P.Value)
log2FC (Prdm16_KO/E)
log2FC (KO vs E)
peak
neighbor
nochange
D
Motifs from SMAD4 peaks
Motifs from pSMAD1/5/8 peaks
Prdm16_E NSCs
SMAD4 (E=1.9e-395)
pSMAD (E=3.3e-56)
RFX (E=5.6e-17)
POU (E=1.1e-5)
FOXP (E=1.1e-3)
pSMAD (E=1.6e-142)
SMAD4/pSMAD (E=1.3e-51)
FOXP (E = 2.3e-19)
SP1 (E=1.4e-18)
TCF3 (E=1.4e-7)
E
Motifs from SMAD4 peaks
Motifs from pSMAD1/5/8 peaks
Prdm16_KO NSCs
SMAD (E=3.5e-236)
AP1 (E=1.3e-51)
FOXP (E=1.1e-5)
SMAD (E=1.6e-142)
AP1 (E=5.7e-33)
FOXP (E=2.3e-19)
STAT (E=1.4e-18)
SP1 (E=6.5e-5)
F
ID3 ectopic
Replicate 1
Replicate 2
Percent of Input
Prdm16_E IgG
Prdm16_E SMAD4
Prdm16_E c-FOS
Prdm16_KO IgG
Prdm16_KO SMAD4
Prdm16_KO c-FOS
G
Wnt7b ectopic
Replicate 1
Replicate 2
Percent of Input
Prdm16_E IgG
Prdm16_E SMAD4
Prdm16_E c-FOS
Prdm16_KO IgG
Prdm16_KO SMAD4
Prdm16_KO c-FOS
H
PRDM16_expressing
PRDM16_KO
PRDM16
SMAD4/pSMAD
AP1

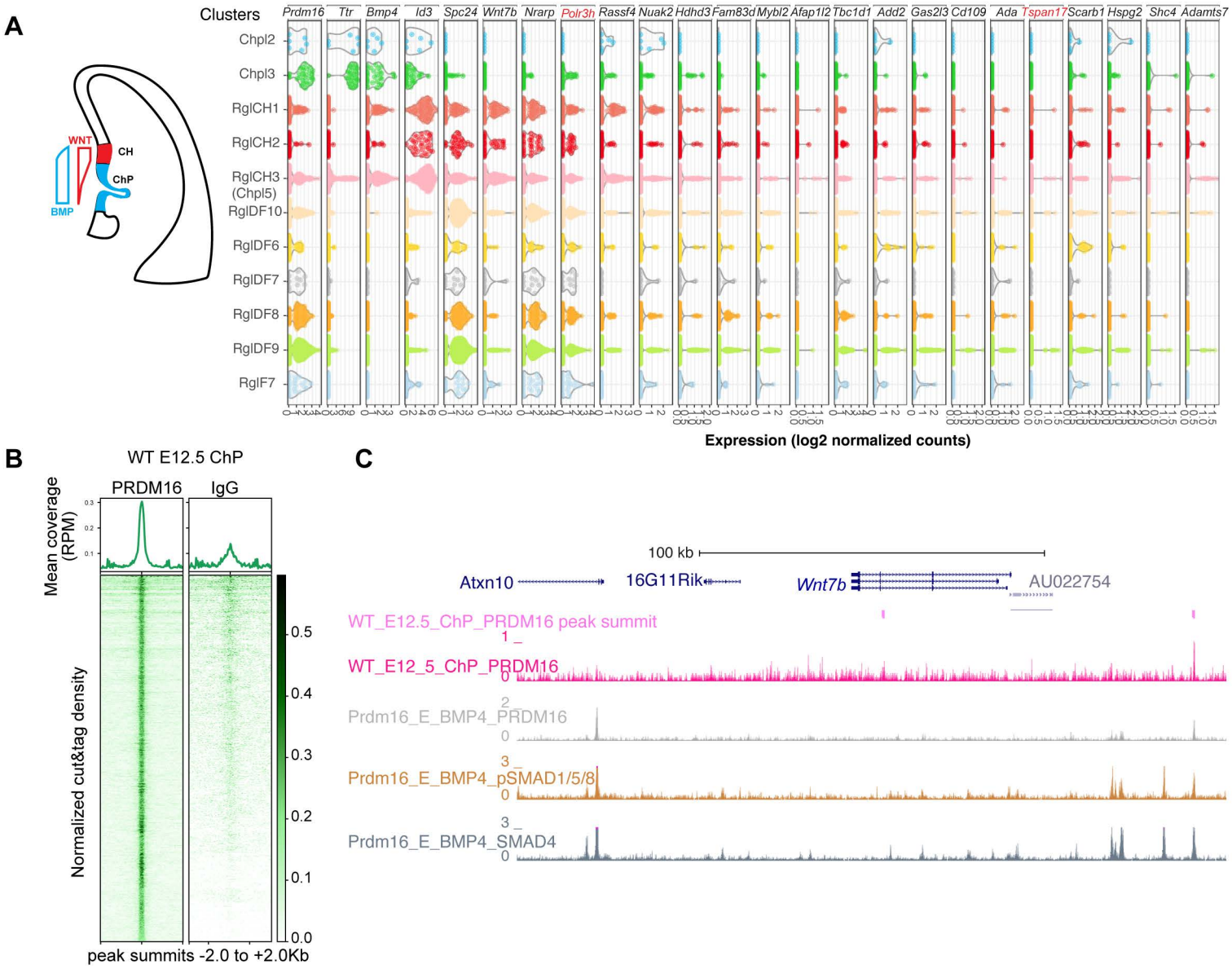
A
Clusters
Prdm16
Ttr
Bmp4
Id3
Spc24
Wnt7b
Nrarp
Polr3h
Rassf4
Nuak2
Hdhd3
Fam83d
Mybl2
Afap1l2
Tbc1d1
Add2
Gas2l3
Cd109
Ada
Tspan17
Scarb1
Hspg2
Shc4
Adamts7
Chpl2
Chpl3
RglCH1
RglCH2
RglCH3
(Chpl5)
RglDF10
RglDF6
RglDF7
RglDF8
RglDF9
RglF7
WNT
CH
ChP
BMP
Expression (log2 normalized counts)
B
WT E12.5 ChP
PRDM16
IgG
Mean coverage
(RPM)
Normalized cut&tag density
peak summits -2.0 to +2.0Kb
C
100 kb
Atxn10
16G11Rik
Wnt7b
AU022754
WT_E12.5_ChP_PRDM16 peak summit
WT_E12_5_ChP_PRDM16
Prdm16_E_BMP4_PRDM16
Prdm16_E_BMP4_pSMAD1/5/8
Prdm16_E_BMP4_SMAD4

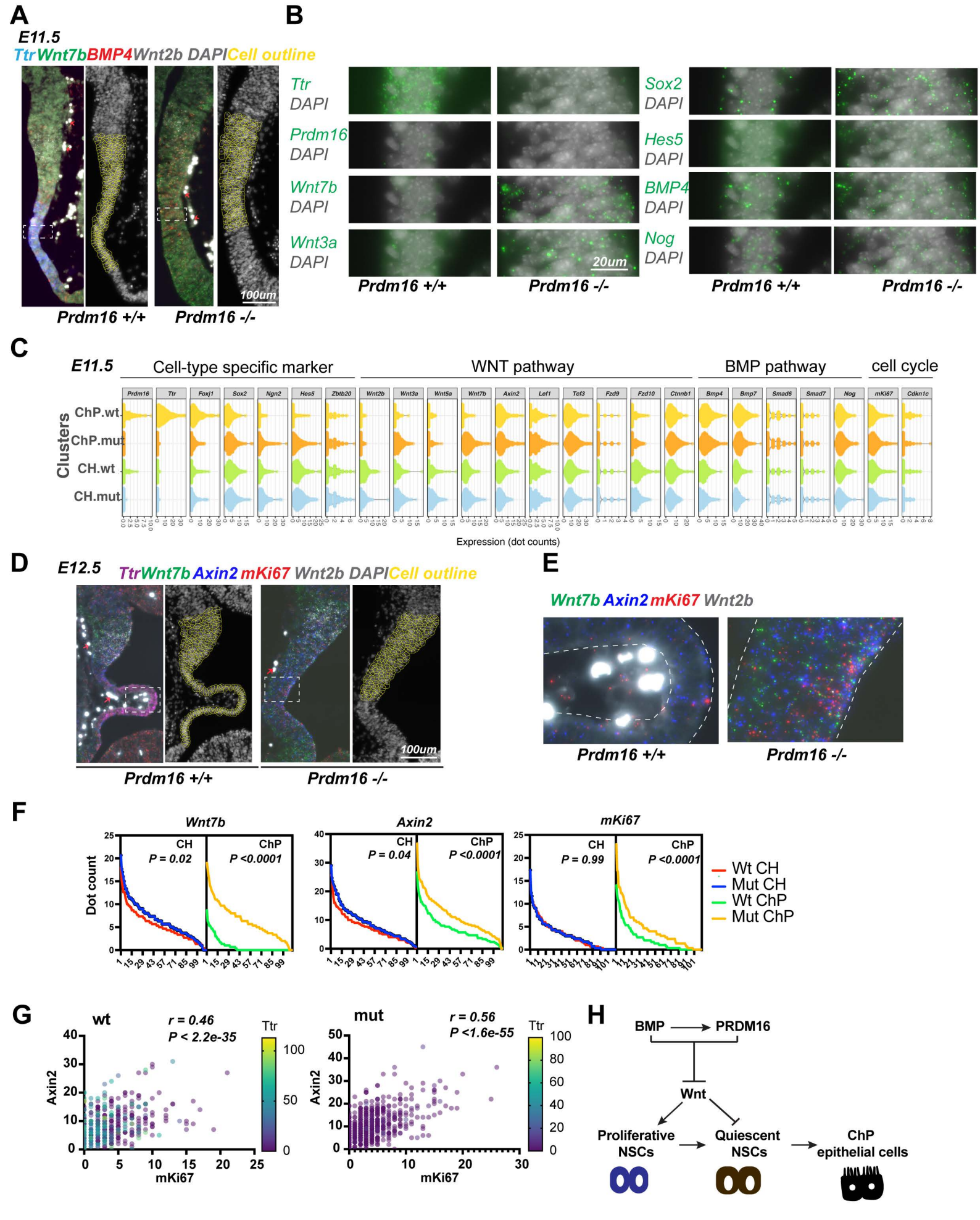
A
E11.5
Ttr Wnt7b BMP4 Wnt2b DAPI Cell outline
100um
Prdm16 +/+
Prdm16 -/-
B
Ttr DAPI
Prdm16 DAPI
Wnt7b DAPI
Wnt3a DAPI
Sox2 DAPI
Hes5 DAPI
BMP4 DAPI
Nog DAPI
20um
Prdm16 +/+
Prdm16 -/-
Prdm16 +/+
Prdm16 -/-
C
E11.5
Cell-type specific marker
WNT pathway
BMP pathway
cell cycle
Prdm16 Ttr Foxj1 Sox2 Ngn2 Hes5 Zbtb20 Wnt2b Wnt3a Wnt5a Wnt7b Axin2 Lef1 Tcf3 Fzd9 Fzd10 Ctnnb1 Bmp4 Bmp7 Smad6 Smad7 Nog mKi67 Cdkn1c
Clusters
ChP.wt
ChP.mut
CH.wt
CH.mut
Expression (dot counts)
D
E12.5
Ttr Wnt7b Axin2 mKi67 Wnt2b DAPI Cell outline
100um
Prdm16 +/+
Prdm16 -/-
E
Wnt7b Axin2 mKi67 Wnt2b
Prdm16 +/+
Prdm16 -/-
F
Wnt7b
Axin2
mKi67
Dot count
CH
P = 0.02
ChP
P <0.0001
CH
P = 0.04
ChP
P <0.0001
CH
P = 0.99
ChP
P <0.0001
Wt CH
Mut CH
Wt ChP
Mut ChP
G
wt
r = 0.46
P < 2.2e-35
Ttr
Axin2
mKi67
mut
r = 0.56
P <1.6e-55
Ttr
Axin2
mKi67
H
BMP
PRDM16
Wnt
Proliferative NSCs
Quiescent NSCs
ChP epithelial cells